Journal of Materials Chemistry C

ROYAL SOCIETY OF CHEMISTRY

PAPER

View Article Online
View Journal | View Issue

Check for updates

Cite this: J. Mater. Chem. C, 2025, 13, 9258

Push–pull carbazole twin dyads as efficient sensitizers/co-sensitizers for DSSC application: effect of various anchoring groups on photovoltaic performance†

Kavya S. Keremane, [ab] Islam M. Abdellah, *[cd] Mohamed R. Eletmany,[de] Praveen Naik, [f] P. Anees[g] and Airody Vasudeva Adhikari *[ah]

To investigate the effect of various anchoring groups of organic sensitizers on fundamental processes occurring inside DSSCs and their overall performance, we designed and synthesized nine new double donor–acceptor (D–A) type organic dyes **DCH$_{1-9}$** comprising carbazole-based twin molecules as electron donors, with a non-conjugated linear alkyl chain as an extended linker featuring multiple acceptor units. Their photophysical, thermal, electrochemical, and theoretical properties were examined to gain a deeper understanding of the structure–property relationship. Photophysical results revealed that all dyes display λ_{abs} and λ_{emi} in the range of 400–470 nm and 500–560 nm, respectively, with a bandgap in the range of 2.46–2.74 eV. The push–pull structure with extended conjugation results in strong fluorescence characteristics. Photophysical and electrochemical studies confirm their thermodynamic feasibility for electron injection, recombination, and dye regeneration in cells. Quantum chemical simulations further provided insights into their structural, electronic, and optical parameters. New DSSCs were fabricated employing dyes **DCH$_{1-9}$** as sensitizers/co-sensitizers. The cell sensitized with **DCH$_1$** achieved the highest power conversion efficiency (PCE) of 2.45% under standard AM 1.5 solar conditions. Furthermore, co-sensitization of **DCH$_{1-9}$** with the Ru-based **HD-2** sensitizer resulted in an improved PCE of 8.82% for **DCH$_2$**, surpassing **HD-2** alone (6.79%). EIS studies were conducted to further explore their energy conversion processes. Conclusively, these investigations highlight the significant potential of dyes carrying carbazole twin molecules with different anchoring units in enhancing the overall performance of DSSCs.

Received 29th October 2024,
Accepted 25th March 2025

DOI: 10.1039/d4tc04612a

rsc.li/materials-c

Open Access Article. Published on 19 1404. Downloaded on 20/11/1404 12:55:10 ..
This article is licensed under a Creative Commons Attribution 3.0 Unported Licence.

Introduction

In the pursuit of clean and solar energy conversion and production from renewable energy resources, dye-sensitized solar cells (DSSCs) have emerged as an important breakthrough because of their potential low processing costs, facile fabrication, and eco-friendly devices.[1,2] These devices are particularly advantageous for dim, diffuse light conversion in indoor applications. Additionally, in non-ideal atmosphere, they generate electricity directly from sunlight due to their partial optical transparency.[3] DSSCs typically consist of a dye-adsorbed mesoporous semiconductor TiO_2 layer deposited on a transparent conducting oxide (FTO) layer, coupled with a platinum counter electrode filled with an electrolyte containing a redox system.[4] Among the four major components of DSSCs, the light-harvesting component photosensitizers (or dyes) play a pivotal role in the overall performance, since it facilitates light absorption and injects the excited electrons into the conduction band of TiO_2.[5,6] An ideal dye must fulfil certain features, such as (i) high photostability,

[a] Organic Materials Laboratory, Department of Chemistry, National Institute of Technology Karnataka, Surathkal, Mangalore-575025, India
[b] Materials Research Institute, The Pennsylvania State University, University Park, PA, 16802, USA
[c] Chemistry Department, Faculty of Science, Aswan University, Aswan, 81528, Egypt. E-mail: islamabdellah2@gmail.com
[d] TECS Department, Wilson College of Textiles, NC State University, Raleigh, 27606, USA
[e] Chemistry Department, Faculty of Science, South Valley University, Qena 83523, Egypt
[f] Department of Chemistry, Nitte Meenakshi Institute of Technology, Yelahanka, Bengaluru, 560064, Karnataka, India
[g] Materials Science Group, Indira Gandhi Centre for Atomic Research, A CI of Homi Bhabha National Institute, Kalpakkam, 603102, Tamilnadu, India
[h] Yenepoya Research Centre, Yenepoya (Deemed to be) University, Deralakatte, Mangalore, 575018, India. E-mail: avachem@gmail.com

† Electronic supplementary information (ESI) available. See DOI: https://doi.org/10.1039/d4tc04612a

This journal is © The Royal Society of Chemistry 2025

Open Access Article. Published on 19 1404. Downloaded on 20/11/1404 12:55:10 ..
This article is licensed under a Creative Commons Attribution 3.0 Unported Licence.

(ii) superior intramolecular charge transfer, (iii) appropriate electronic energy between HOMO and LUMO levels, (iv) favourable anchoring group to firmly bind on TiO_2, (v) rapid electron injection to TiO_2 and reduced recombination, and (vi) broad structural diversity.[7,8]

Over the last three decades, organic dyes featuring donor–acceptor (D–A) or donor–π–acceptor (D–π–A) motifs have been widely studied, particularly those with carbazole cores due to their excellent charge-transport properties, energy levels, and stability.[9–11] Carbazole-based di-anchoring dyes, such as A–D–π–A, A–π–D–π–A configurations, have shown great promise in DSSCs due to their multi-binding ability, increased dye loading, and enhanced electron extraction, which leads to improved device performance.[12–15] Dyes with double donor–acceptor units and extended alkyl chain linkers have proven to be more effective than single donor–acceptor dyes, as they suppress dark currents, increase light absorption efficiency, and improve the electron injection and lifetime.[16–22] Twin molecules with non-conjugated alkyl chains have demonstrated state-of-the-art performance due to their better solubility and improved pore-filling in mesoporous TiO_2.

In general, the efficiency of DSSCs largely depends on the interaction between the dye and the TiO_2 semiconductor surface.[14,23–27] A strong electronic overlap between the two ensures rapid charge transfer, making the anchoring group crucial for binding the dye to the TiO_2 layer. Thus, the anchoring group plays a pivotal role. Different anchoring groups, such as carboxylic, cyanoacrylic, rhodamine-3-acetic acid, and phosphonic acids, have been explored to understand their impact on dye binding, electron injection, and long-term stability.[28–31] Among all, cyanoacrylic acid (CAA) is widely recognized as an effective anchoring group. However, exploring dyes with alternative anchoring or electron-withdrawing groups remains essential for advancing this technology. Despite this need, very few studies have systematically compared the impacts of different anchoring groups on dye aggregation, electron injection, and recombination kinetics in dual donor–acceptor dyes with extended linkers. In this context, it is necessary to compare the effect of various anchoring groups to address the undesirable processes above in solar cells.[32–35] The primary objective of our study is to systematically evaluate different anchoring groups beyond the commonly used CAA, and assess their influence on the photophysical and electrochemical properties. Our findings contribute to a broader understanding of how alternative anchoring groups, including rhodanine-3-acetic acid and barbituric acid derivatives can be optimized for DSSCs.[36–38] Each new anchoring group brings the potential for unique electronic interactions with the semiconductor surface, which could optimize electron injection or reduce charge recombination in ways not achievable with traditional groups. Exploring new groups also enables tailored designs for specialized applications, such as indoor photovoltaics or building-integrated systems. This pursuit expands the versatility, efficiency, and sustainability of DSSCs, while still acknowledging the value of established moieties.

Furthermore, concerted companion (CC) dyes have emerged as a promising approach to enhance the DSSC efficiency by linking two complementary dye units to achieve broad absorption and improved photovoltaic performance.[39] As an emerging class of di-branched dyes, CC dyes have been designed to enhance the DSSC efficiency by linking porphyrin and organic sub-dye units. The intramolecular engineering of CC dyes simplifies the adsorption process while enhancing the efficiency and stability. Di-branched dyes, which integrate porphyrin and organic dye subunits, have demonstrated superior light-harvesting capabilities. Notably, the incorporation of wrapped porphyrin dye units has led to the development of doubly concerted companion (DCC) effects, further improving the performance. For instance, Xie *et al.* reported on a series of CC dyes, where an optimized linker length improved the molecular orientation and resulted in a PCE of up to 12.4% after coadsorption with CDCA.[40–42] In addition to the excellent efficiency, this strategy shows the advantages of avoiding the competitive adsorption problem and time-consuming optimization of the dye adsorption process. Additionally, double-anchored dyes exhibit stronger adsorption, enhancing cell stability, with less than 10% PCE loss after 1000 hours of light exposure, making them a superior alternative to traditional DSSC dyes. Moving forward, the co-sensitization and CC dye strategies should be further explored to achieve enhanced panchromatic absorption, particularly in the near-infrared (NIR) region.[43,44]

Co-sensitization is another way to optimize the performance of DSSCs.[45] It is a key strategy to overcome the limitations of using a single dye in the cell, as organic dyes often have narrow absorption spectra and limited photon-harvesting capabilities.[46] By combining two or more dyes, the overall light-harvesting ability can be enhanced. For example, Ru(II) dyes, which have lower absorption in the higher wavelength region, can be complemented by dyes with higher molar extinction coefficients, improving light absorption and boosting power conversion efficiency (PCE).[47,48] To meet the stringent requirements of high-performance sensitizers, Nazeeruddin *et al.*[49] successfully developed a panchromatic ruthenium complex, known as black dye, incorporating carboxylated terpyridyl and three thiocyanate ligands, achieving a power conversion efficiency (PCE) of 10.4%. Similarly, DSSCs employing the widely used N719 sensitizer, demonstrated PCEs exceeding 9.18% under AM 1.5 sunlight. Wang *et al.* later introduced K19, an amphiphilic ruthenium complex, which exhibited a PCE of 7.0%.[50]

In recent years, extensive research efforts have been directed toward the development of efficient sensitizers based on organic frameworks, zinc porphyrins, and ruthenium complexes. Notably, porphyrin-based dyes have achieved efficiencies above 13%, making them promising candidates for DSSCs.[51,52] However, porphyrin dyes inherently suffer from limited absorption in the UV, green, and near-infrared (NIR) regions, which restricts their overall efficiency. For successful co-sensitization, the energy levels (HOMO and LUMO) of the dyes must align to ensure efficient electron injection into the TiO_2 conduction band and smooth dye regeneration. We selected **HD-2** dye for co-sensitization due to its broad absorption, stability, efficient charge transfer, and strong anchoring properties.[53]

Open Access Article. Published on 19 1404. Downloaded on 20/11/1404 12:55:10 ..
This article is licensed under a Creative Commons Attribution 3.0 Unported Licence.

The chemical stability of **HD-2** and its ability to complement organic or metal-free dyes enhance the performance of DSSCs by improving light harvesting, reducing recombination, and increasing overall efficiency. Recent studies show that co-sensitization with donor–acceptor organic dyes and Ru-based complexes leads to enhanced photovoltaic performance. This improvement is attributed to better adsorption into the pores of TiO_2, where bulky ruthenium dyes struggle. Understanding the role of simple co-sensitizers and optimizing interfacial charge transfer are crucial for maximizing the DSSC efficiency.[54–58]

Encouraged by this, in order to enhance the light-harvesting units and broaden the absorption spectra, in the present study we have designed nine novel dual D–A configured organic dyes **$DCH_{1–9}$**, carrying twin carbazole units as an effective electron donor, and cyanoacetic acid (**DCH_1**), rhodanine-3-acetic acid (**DCH_2**), rhodamine (**DCH_3**), barbituric acid (**DCH_4**), 1,3-dimethylbarbituric acid (**DCH_5**), 1,3-diethyl-2-thiobarbituric acid (**DCH_6**), 2,4-thiazolidinedione (**DCH_7**), oxindole (2-indolone) (**DCH_8**), and 4-nitrophenyl acetonitrile (**DCH_9**) groups were employed as an electron acceptor/anchoring units, while molecular designing. The bridged non-conjugated linear alkyl chain of double-branched dyes facilitates higher surface coverage on TiO_2 films, influencing the overall performance of solar cell.

These final molecules were synthesized in good yields by adopting simple synthetic protocols, *viz.*, *N*-alkylation, Vilsmeier–Hack reaction, followed by Knoevenagel condensation reactions (Scheme 1), and the respective structures are shown in Fig. 1. The target molecules and intermediates were well characterized using elemental analyses and different spectroscopic techniques. The photophysical and electrochemical characterization, including energy conversion (ΔG_{inj}, ΔG_{rec}, and ΔG_{reg}), were evaluated using UV-visible absorption/photoluminescence (PL) studies and cyclic voltammetric (CV) studies, respectively. Furthermore, the thermal stability of synthesized dyes was evaluated using TGA and DSC studies. Density functional theory (DFT) and time-dependent density functional theory (TD-DFT) were also used to investigate the molecular geometry, electron distributions, absorption and charge-transfer

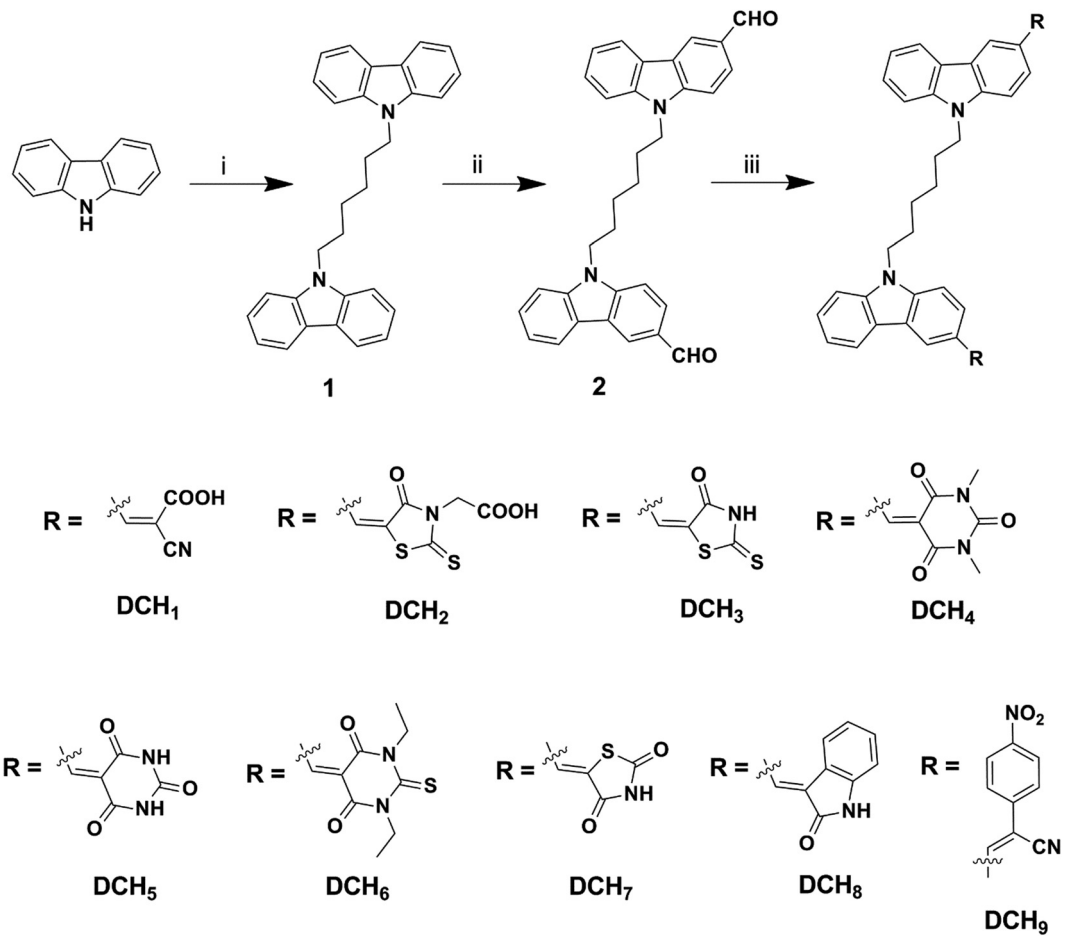

Scheme 1 Synthetic routes for the dyes **$DCH_{1–9}$**: (i) 1,6-dibromohexane, NaH, DMF, RT, 12 h; (ii) $POCl_3$, DMF, 110 °C, 2 h; (iii) **DCH_1**: cyanoacetic acid, ammonium acetate, glacial CH_3COOH, 110 °C, 12 h; **DCH_2**: rhodanine-3-acetic acid, ammonium acetate, glacial CH_3COOH, 110 °C, 12 h; **DCH_3**: rhodanine, ammonium acetate, glacial CH_3COOH, 110 °C, 12 h; **DCH_4**: 1,3-dimethylbarbituric acid, methanol, 60 °C, 10 h; **DCH_5**: barbituric acid, methanol, 60 °C, 10 h; **DCH_6**: 1,3-diethyl-2-thiobarbituric acid, methanol, 60 °C, 10 h; **DCH_7**: 2,4-thiazolidinedione, ammonium acetate, glacial CH_3COOH, 110 °C, 12 h; **DCH_8**: oxindole, pipyridine, ethanol, 80 °C, 12 h; **DCH_9**: 4-nitrophenyl acetonitrile, potassium *tert*-butoxide, methanol, 60 °C, 6 h.

 This journal is © The Royal Society of Chemistry 2025

Open Access Article. Published on 19 1404. Downloaded on 20/11/1404 12:55:10 ..
This article is licensed under a Creative Commons Attribution 3.0 Unported Licence.

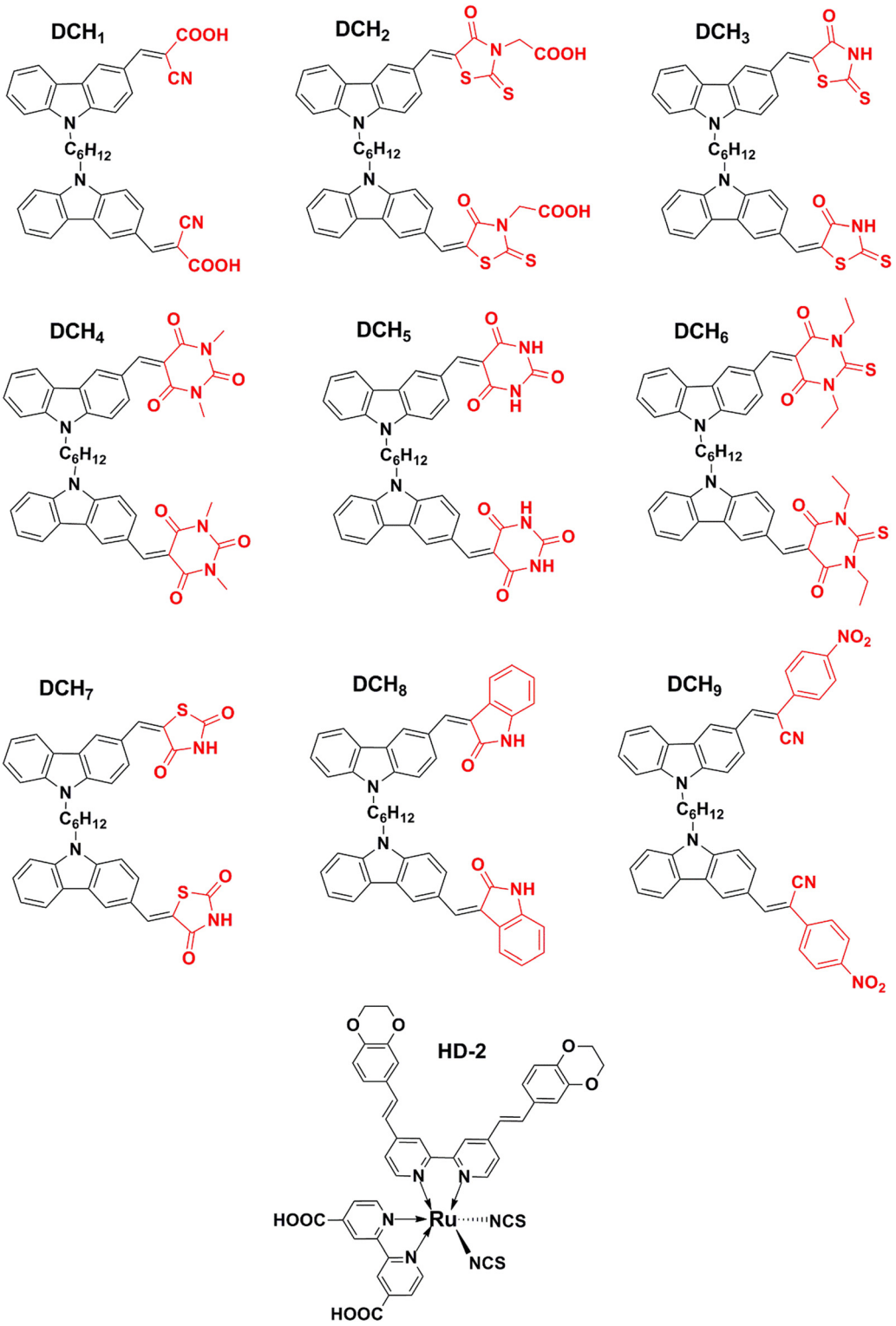

Fig. 1 Chemical structures of the dual donor–acceptor configured new dyes **DCH$_{1-9}$** and the benchmark reference dye **HD-2**.

mechanism, electrostatic potential (ESP), and density of states (DOS) of the synthesized dyes theoretically using Turbomole 7.2 V and VASP software. Eventually, the dyes **DCH$_{1-9}$** were employed as sensitizers and co-sensitizers with Ru(II) based **HD-2** dye towards the DSSC fabrication, and their photovoltaic performance data were investigated. Finally, electrochemical impedance spectroscopy (EIS) studies were carried out to understand their interfacial charge recombination and carrier transportation processes (R_S, R_{CT}, and R_{Pt}) in depth with respect to both sensitization and co-sensitization processes.

Open Access Article. Published on 19 1404. Downloaded on 20/11/1404 12:55:10 ..
This article is licensed under a Creative Commons Attribution 3.0 Unported Licence.

Results and discussion

Synthesis and characterization

The synthetic pathways of seven new metal-free organic dyes **DCH$_{1-9}$** are shown in Scheme 1. The requisite intermediate 1,6-di(9*H*-carbazole-9-yl)hexane (**1**) was obtained from 9*H*-carbazole by treating it with 1,6-dibromohexane in the presence of a strong base, *i.e.*, sodium hydride. This was converted to the key precursor 9,9′-(hexane-1,6-diyl)bis(9*H*-carbazole-3-carbaldehyde) (**2**) through the Vilsmeier–Hack reaction protocol with good yield. In the final step, the target molecules **DCH$_{1-9}$** were obtained by following the Knoevenagel condensation protocol, wherein the precursor **2** was condensed with various active methylene compounds. All the synthesized compounds were further purified using the typical recrystallization and chromatographic techniques. The molecular structures of these target compounds and their intermediates were established by using different spectroscopy tools. Their spectra are displayed in S1–S39 of ESI.†

Theoretical studies

To gain deeper insight into the molecular structure, electronic distribution, and frontier molecular orbitals of **DCH$_{1-9}$**, molecular orbital calculations were performed using the density functional theory (DFT). All the theoretical calculations were executed using the Turbomole 7.2 software package. The ground-state geometries of the synthesized dye molecules in a gas phase were optimized based on a semiempirical AM1 basis with MOPAC in Tmolex.[59,60] The aforementioned geometries were further optimized using C_1 point group symmetry *via* Becke's three-parameter hybrid functional and Lee–Yang–Parr's gradient-corrected correlation functional (B3LYP) program and basic set def-TZVPP.[61] The optimized geometries of dyes **DCH$_{1-9}$** are given in Fig. S40 (ESI†). The geometry of the twin carbazole unit in each dye was not precisely planar, but rather slightly tilted in the middle with a butterfly shape. Therefore, the non-planar geometry of the carbazole ring can help to suppress the dye aggregation on the TiO_2 surface. The electronic density distributions in the HOMO and LUMO levels of the nine different dyes **DCH$_{1-9}$**, along with their bandgaps, are shown in Fig. 2 and the corresponding data are tabulated in Table 1. Furthermore, to understand the adsorption and charge-transfer mechanism in the presence of a supporting substrate, density functional theory (DFT) calculations were performed using the Vienna *Ab initio* Simulation Package (VASP). The **DCH$_1$** dye interaction with the TiO_2 semiconductor is shown in Fig. S41 (details can be found in ESI†). Evaluating the FMO distribution allows for a qualitative prediction of a dye's effectiveness in DSSCs. It is equally important to analyze the molecular orbitals adjacent to the FMOs, as they significantly influence the spectral behavior of the dye molecules. A LUMO distribution localized on the acceptor moiety is particularly advantageous, as it helps the sensitizer to anchor more effectively to the TiO_2 surface, facilitating intramolecular charge transfer. The band-gap energy plays a crucial role in determining the dye's photocurrent, as it governs the absorption of light at relevant wavelengths. Efficient HOMO and LUMO separation promotes effective charge separation, unlike insufficiently separated HOMO−1 and LUMO+1 distributions, ensuring better electron transfer and overall DSSC performance. As seen from Fig. 2, the electrons at the highest occupied molecular orbital (HOMO) levels are mainly populated on the carbazole donor unit, whereas the electron density distribution in the lowest unoccupied molecular orbital (LUMO) is sizably delocalized through the acceptor part of **DCH$_{1-9}$**. The LUMO and LUMO+1 levels of the dye molecules are largely

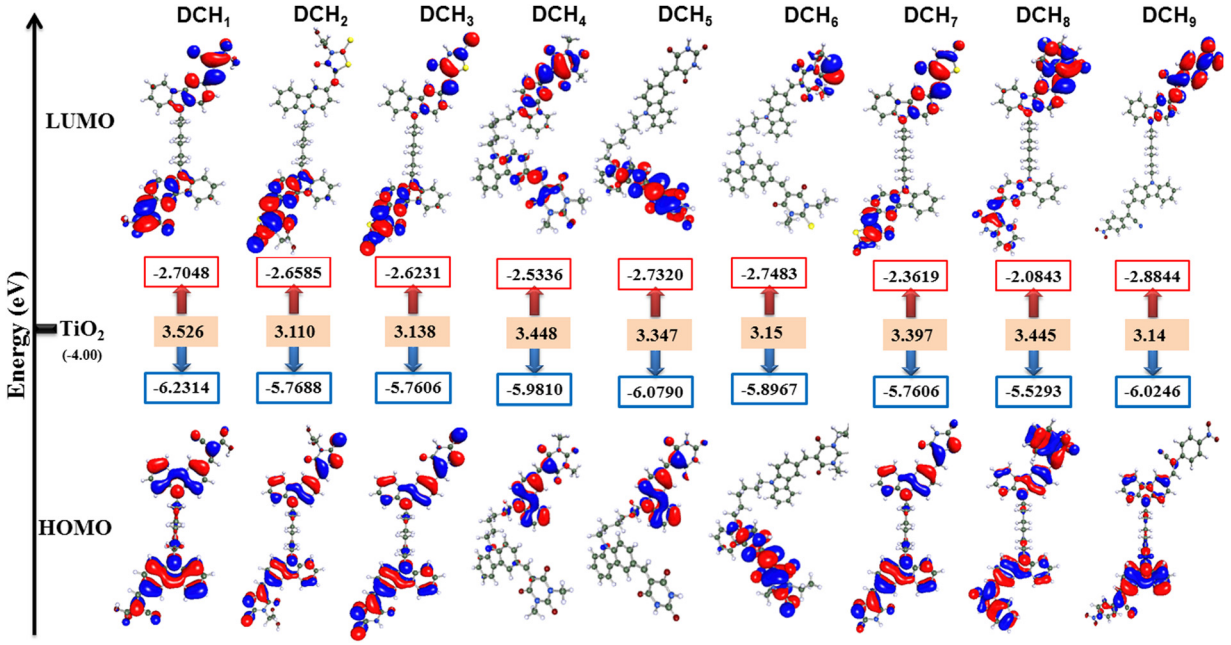

Fig. 2 The electronic cloud distributions in the FMO levels of dyes **DCH$_{1-9}$**.

 This journal is © The Royal Society of Chemistry 2025

Table 1 Theoretical electrochemical data of dyes **DCH$_{1-9}$**

Parameters	**DCH$_1$**	**DCH$_2$**	**DCH$_3$**	**DCH$_4$**	**DCH$_5$**	**DCH$_6$**	**DCH$_7$**	**DCH$_8$**	**DCH$_9$**
E_{HOMO} (eV)	−6.23	−5.76	−5.76	−5.98	−6.07	−5.89	−5.76	−5.52	−6.02
E_{LUMO} (eV)	−2.70	−2.65	−2.62	−2.53	−2.73	−2.74	−2.36	−2.08	−2.88
E_g[a] (eV)	3.52	3.11	3.13	3.44	3.34	3.15	3.39	3.44	3.14

[a] These values were obtained from DFT calculations in a vacuum.

Open Access Article. Published on 19 1404. Downloaded on 20/11/1404 12:55:10 ..
This article is licensed under a Creative Commons Attribution 3.0 Unported Licence.

dispersed on cyanoacetic acid, while the majority of the HOMO energy levels are delocalized on the electron-donating unit. The closely overlapping HOMO–LUMO orbitals act as a channel for a quick ICT process. Thus, there is a clear electron cloud movement from the donor moiety towards the anchoring unit, facilitating an efficient photoinduced interfacial electron transfer from LUMO to the semiconductor electrode through effective intramolecular charge separation under light irradiation.

The theoretical HOMO energy levels obtained for dyes **DCH$_{1-9}$** are −6.231 (**DCH$_1$**), −5.768 (**DCH$_2$**), −5.760 (**DCH$_3$**), −5.981 (**DCH$_4$**), −6.079 (**DCH$_5$**), −5.896 (**DCH$_6$**), −5.760 (**DCH$_7$**), −5.529 (**DCH$_8$**), and −6.024 (**DCH$_9$**), respectively, which are significantly lower than that of the redox potential of the I_3^-/I^- electrolyte system (−5.2 eV), confirming that the synthesized dyes can undergo a quick ground-state regeneration process. The theoretical LUMO energy levels obtained for dyes **DCH$_{1-9}$** are −2.704 (**DCH$_1$**), −2.658 (**DCH$_2$**), −2.623 (**DCH$_3$**), −2.533 (**DCH$_4$**), −2.732 (**DCH$_5$**), −2.748 (**DCH$_6$**), −2.361 (**DCH$_7$**), −2.084 (**DCH$_8$**), and −2.884 (**DCH$_9$**), respectively, which are significantly higher than the conduction band (CB) of TiO_2 (–4.2 eV), indicating their fast electron injection. The theoretical bandgap obtained for dyes **DCH$_{1-9}$** are 3.52 (**DCH$_1$**), 3.11 (**DCH$_2$**), 3.13 (**DCH$_3$**), 3.44 (**DCH$_4$**), 3.34 (**DCH$_5$**), 3.15 (**DCH$_6$**), 3.39 (**DCH$_7$**), 3.44 (**DCH$_8$**), and 3.14 (**DCH$_9$**), respectively, which may be due to the different anchoring abilities of the molecules. Conclusively, the well-overlapped HOMO and LUMO orbitals of the dyes **DCH$_{1-9}$** can guarantee a superior charge transfer and the efficient interfacial injection of electrons from the excited state of the dye molecule into the conduction band of the TiO_2 semiconductor.

In addition, the electronic excited state properties of materials were studied in depth using the time-dependent density functional theory (TD-DFT) method in the presence of time-dependent perturbations. According to the adiabatic approximation, the temporal nonlocality is neglected and an assumption is made that at any point of time, the exchange–correlation (xc) functional depends exclusively on the instantaneous density.[62] Based on the aforesaid approximation, time-dependent perturbations can be applied to the xc functional derived for ground-state DFT, *i.e.*, BP (Beck–Perdew) and hybrid functional (B3LYP). In TD-DFT calculations, the accuracy of the assimilated results mainly relies on the functional and basis set employed for the calculations.[63]

Fig. S42 (ESI†) displays the theoretically simulated absorption spectra of the dyes **DCH$_{1-9}$**, obtained by employing the B3LYP functional and def-TZVP basis set. The adiabatic approximation states that the TD-DFT temporal nonlocality is ignored, and that the exchange–correlation (xc) component solely depends on the instantaneous density at any given moment.[64] Therefore, the hybrid functional (B3LYP) and BP (Beck–Perdew) as xc functionals were derived for ground-state DFT. The correctness of assimilation findings in TD-DFT computations is typically determined by the basic set employed for the calculations. The theoretically calculated absorption maxima (λ_{max}) of the investigated molecules **DCH$_{1-9}$** are summarized in Table 1. Furthermore, the simulated spectra of **DCH$_{1-9}$** depict two distinct peaks in the spectrum, belonging to the mixed π–π* transition and charge-transfer process within the molecules, which help to predict the energies related to long-range charge-transfer states.

In all of the synthesized molecules, a strong intra-dye electronic excitation occurs, owing to the HOMO → LUMO transitions. Here, the excitations at the longer wavelengths are due to the electronic transitions from the HOMO to LUMO+1 and LUMO+3. Accordingly, the lower-energy excitations are ascribed to intramolecular charge transfer (ICT) transitions from **DCH$_{1-9}$** to TiO_2. These exactitudes of the TD-DFT results illustrate that the functional and basis set chosen for the studies are in accordance with the experimentally obtained results. From the TD-DFT results, it is clear that the functional and basis sets used for the investigations are in good agreement with the outcomes of the experimental results. The theoretically simulated IR-absorption spectra of **DCH$_{1-9}$** are displayed in Fig. S43 (ESI†). As expected, both the simulated and experimentally obtained results are in good agreement with each other.

To investigate the distribution of total charge density around the dye molecules, electrostatic potential (ESP) maps of **DCH$_{1-9}$** have been generated, as illustrated in Fig. 3. This analysis explores the ESP to predict the physicochemical properties, focusing on regions of electrophilic and nucleophilic attack and areas of electrostatic potential. The three-dimensional visualization of the ESP plot provides a better understanding of the electrostatic influence of the molecules.[55] The molecular electrostatic potential, which is linked to electron density, plays a key role in understanding hydrogen bonding interactions, as well as the reactivity of electrophilic and nucleophilic sites. The cavity boundaries in the molecules resemble the density isosurface in the ESP plot, reflecting the total charge distribution, including electronegativity, dipole moment, and sites of chemical reactivity. The electrostatic potential values are color-coded in increasing order as follows: blue > green > yellow > orange > red.[11] In these plots, electron-rich regions are indicated in red, while electron-deficient regions are shown in blue. This induces positive and negative charges on the cavity surface, creating local electric fields within the cavity. Green represents regions of zero electrostatic potential.

Open Access Article. Published on 19 1404. Downloaded on 20/11/1404 12:55:10 ..
This article is licensed under a Creative Commons Attribution 3.0 Unported Licence.

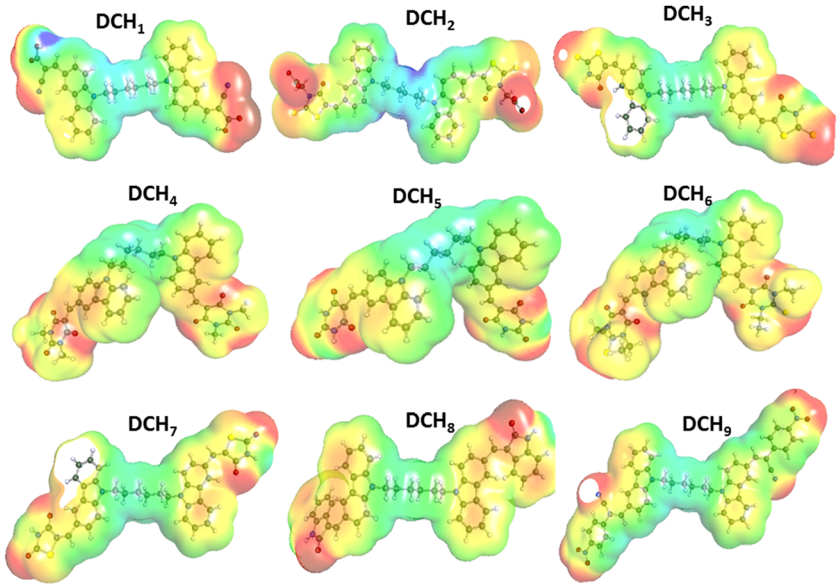

Fig. 3 Molecular electrostatic potential (ESP) mapping on the isodensity surface of dyes **DCH$_{1-9}$**.

The ESP surfaces reveal both positive and negative regions: the positive regions are preferred sites for nucleophilic attacks, while the negative regions are more suitable for electrophilic attacks.[63] From Fig. 3, it is clear that in dyes **DCH$_{1-2}$**, the electron density is primarily concentrated on the cyanovinylene and carbonyl groups of cyanoacetic acid. In contrast, in **DCH$_3$**, **DCH$_7$**, and **DCH$_8$**, the electron density is focused on the thioketone and carbonyl groups of rhodanine derivatives and oxindole. For **DCH$_{4-6}$**, the electron density is primarily located on the carbonyl groups of barbituric acid and its derivatives. Additionally, the positive region in **DCH$_{1-9}$** is localized on the carbazole rings, indicating that these groups can act as efficient donors and are attractive sites for nucleophilic attacks. On the other hand, the acceptor groups, located on the opposite side of the molecule, are surrounded by regions of zero potential, suggesting vulnerability to electrophilic attacks.

Overall, the ESP plots clearly illustrate the movement of electron density from the donor moiety to the anchoring unit *via* spacer units, facilitating effective electron transfer in **DCH$_{1-9}$**. This observation makes these dyes promising candidates for use as sensitizers in dye-sensitized solar cells (DSSC).

According to quantum mechanics, the density of states (DOS) of a system primarily refers to the number of available energy levels per unit energy increment. It represents the number of states available for occupation within a specific energy range.[29,33] A high DOS value at a given energy level indicates that many states are available for occupation, while a zero DOS signifies that no free states are available at that energy level. In essence, DOS provides an average over time and space within the system, and describes the contribution of different orbitals across a range of energies. Moreover, DOS is crucial for understanding the charge transfer between molecules and the TiO_2 semiconductor, which generates dipolar fields at the TiO_2/material interface, ultimately tuning the band energy levels. A material with a smaller bandgap can facilitate faster electron transport, enhancing the driving force for rapid charge injection at the interface.[32,55] The DOS plots of **DCH$_{1-9}$**, shown in Fig. S44 (ESI†), illustrate how different orbitals contribute as the energy increases. The figure shows that as the energy rises, the contribution of p-orbitals becomes more dominant compared to s-orbitals. Additionally, the p-orbitals of oxygen and nitrogen atoms play a significant role in binding the dye to TiO_2. All newly synthesized molecules exhibit similar DOS patterns, suggesting they meet the necessary criteria. Furthermore, the DOS spectra of the dyes show no significant energy gaps, but the results are consistent with existing literature. All dyes (**DCH$_{1-9}$**) demonstrate significant charge transfer from the donor to the acceptor unit, confirming that they fulfill the basic requirements of an ideal sensitizer.

Photophysical properties

The UV-vis absorption spectra of double D–A dyes (**DCH$_{1-9}$**) were measured in *N*,*N*-dimethyl formamide (DMF) solution at 10^{-5} M conc. at room temperature (Fig. 4(a)), and the corresponding spectral parameters are summarized in Table 2. All the dyes showed two distinct strong and broad absorption spectra in the ultraviolet and visible regions. The lower absorption band in the region of 280–370 nm is ascribed to the π–π* electronic excitation of conjugated molecules, whereas the higher absorption band (402–468 nm) is assigned to the intramolecular charge transfer (ICT) between the donor and acceptor unit. As shown in Fig. 4(a), the observed major λ_{max} at 402 nm (**DCH$_1$**), 422 nm (**DCH$_2$**), 421 nm (**DCH$_3$**), 450 nm (**DCH$_4$**), 445 nm (**DCH$_5$**), 468 nm (**DCH$_6$**), 397 nm (**DCH$_7$**), 419 nm (**DCH$_8$**), and 440 nm (**DCH$_9$**) are attributed to mixed intramolecular charge transfer (ICT)/π–π* transition of the chromophores, which was further confirmed by TD-DFT calculations.[55] From the results, we emphasize that the λ_{abs} of

 This journal is © The Royal Society of Chemistry 2025

Open Access Article. Published on 19 1404. Downloaded on 20/11/1404 12:55:10 ..
This article is licensed under a Creative Commons Attribution 3.0 Unported Licence.

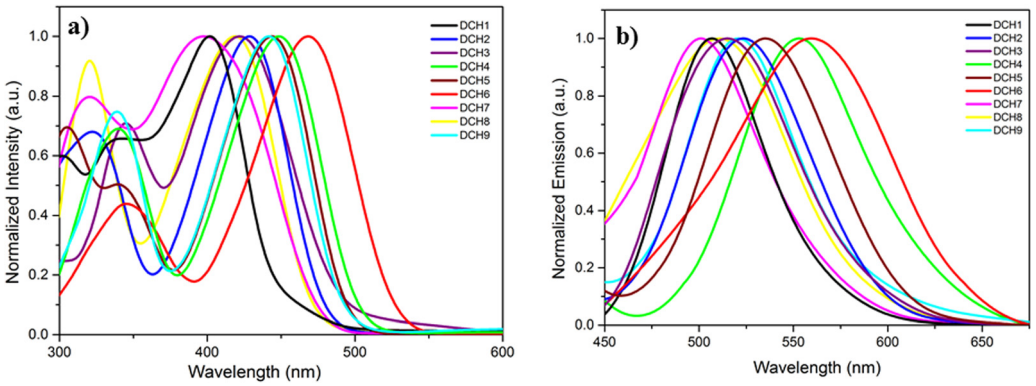

Fig. 4 (a) Normalized UV-Vis absorption and (b) fluorescence emission spectra of **DCH$_{1-9}$** recorded in 10^{-5} M DMF solution under ambient atmosphere.

Table 2 Photophysical and thermal characterization data of dyes **DCH$_{1-9}$**

Parameters	**DCH$_1$**	**DCH$_2$**	**DCH$_3$**	**DCH$_4$**	**DCH$_5$**	**DCH$_6$**	**DCH$_7$**	**DCH$_8$**	**DCH$_9$**
$\lambda_{abs}{}^a$ (nm)	402	422	421	450	445	468	397	419	440
$\lambda_{emi}{}^a$ (nm)	510	530	516	553	535	562	500	512	524
Stokes shift^a (cm^{-1})	5275	4896	4260	4142	3782	3577	5188	4336	4080
ε (M^{-1} cm^{-1}) at $\lambda_{abs}{}^a$ (nm)	20 760	25 393	24 707	17 930	20 076	16 468	23 617	19 738	14 720
$E_{0-0\ opt}{}^b$ (eV)	2.74	2.70	2.65	2.64	2.56	2.46	2.73	2.62	2.61
$T_m{}^c$ (°C)	281	334	294	205	216	291	330	259	191
$T_d{}^c$ (°C)	315	340	326	302	307	318	336	310	258

^{a} Absorption and emission spectra measured in DMF (at concentration of 10^{-5} M) at room temperature. ε (M^{-1} cm^{-1}): molar extinction coefficient. ^{b} Optical band gap E_{0-0} is the voltage of the intersection point between the absorption and emission spectra. ^{c} T_d decomposition temperature observed from TGA 5% of weight loss at 10 °C min^{-1} and T_m observed from DSC at 10 °C min^{-1} under nitrogen atmosphere.

organic sensitizers **DCH$_{4-6}$** show a bathochromic shift when compared to the other dyes. The dye **DCH$_6$** exhibits a significantly broader and more intense absorption than other dyes, likely due to its extended conjugation and enhanced light-harvesting ability, which is attributed to the presence of the strong electron-withdrawing 1,3-diethyl-2-thiobarbituric acid group. This group is a potent electron acceptor because the sulfur (S) atom in its structure increases the electron-accepting efficiency compared to the oxygen (O) atom in conventional barbituric acid. The sulfur substitution lowers the energy gap for electronic transitions, causing a redshift in the absorption peak. Additionally, the higher polarizability of sulfur improves the charge-transfer efficiency, contributing to the broader absorption profile by making the electronic transitions more accessible.

The fluorescence emission spectra of the dyes **DCH$_{1-9}$** are recorded in DMF solution at 10^{-5} M concentration by exciting at their respective absorption maxima. Fig. 4(b) represents the normalized emission spectra of synthesized dyes **DCH$_{1-9}$**, and their resultant spectral parameters are tabulated in Table 2. All the dye molecules exhibit a characteristic single emission band in the region of 500–562 nm region. The molecule **DCH$_6$** displays λ_{emi} of 562 nm, which is slightly more redshifted than that of **DCH$_1$** (510 nm), **DCH$_2$** (530 nm), and **DCH$_3$** (516 nm), **DCH$_4$** (553 nm), **DCH$_5$** (535 nm), **DCH$_7$** (501 nm), **DCH$_8$** (512 nm), and **DCH$_9$** (524 nm), respectively, which may be due to the presence of strong electron-withdrawing 1,3-diethyl-2-thiobarbituric acid. The observed shift is desirable as it escalates the light-harvesting nature of the sensitizer in the visible region. Furthermore, we calculated the Stokes shift values of the dyes. The values are listed in an increasing order of **DCH$_6$** (3577 cm^{-1}) < **DCH$_5$** (3582 cm^{-1}) < **DCH$_9$** < (4080 cm^{-1}) < **DCH$_4$** (3577 cm^{-1}) < **DCH$_3$** (4260 cm^{-1}) < **DCH$_8$** (4336 cm^{-1}) < **DCH$_2$** (4896 cm^{-1}) < **DCH$_7$** (5188 cm^{-1}) < **DCH$_1$** (5275 cm^{-1}), respectively. It is noted that the Stokes shift values of the barbituric acid derivatives are smaller than that of the cyanoacetic acid and rhodanine derivatives, which could have resulted from the higher planarity, also illustrating smaller conformational changes in the excited state.[29] The dye **DCH$_1$** displayed the highest value of Stokes shift, which may be caused by large changes in the dipole moment in the excited state, as a result of charge transfer from the donor to the acceptor moiety. Additionally, the optical bandgap values of the synthesized dyes were calculated from the obtained absorption and emission spectral data. The acquired bandgaps of **DCH$_{1-9}$** decrease in the following order: 2.74 eV (**DCH$_1$**) > 2.73 eV (**DCH$_7$**) > 2.70 eV (**DCH$_2$**) > 2.65 eV (**DCH$_3$**) > 2.64 eV (**DCH$_4$**) > 2.62 eV (**DCH$_8$**) > 2.61 eV (**DCH$_9$**) > 2.56 eV (**DCH$_5$**) > 2.46 eV (**DCH$_6$**). Furthermore, the molar absorption coefficients (ε) of the ICT bands were calculated, and are in the range of 14 720 M^{-1} cm^{-1} to 25 396 M^{-1} cm^{-1}. Among all, the dye **DCH$_2$** showed the highest 'ε' value, indicating enhanced light-harvesting ability of the strong electron-withdrawing rhodanine-3-acetic acid unit in the visible region, which could produce greater short-circuit current and thus show improved performance.

Open Access Article. Published on 19 1404. Downloaded on 20/11/1404 12:55:10 ..
This article is licensed under a Creative Commons Attribution 3.0 Unported Licence.

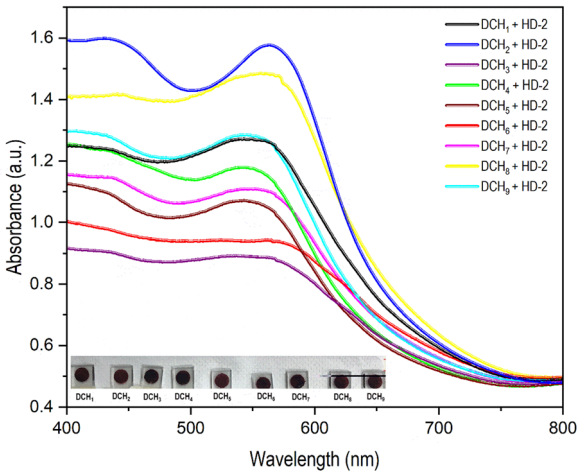

Fig. 5 UV-vis absorption spectra of **DCH$_{1-9}$** + **HD-2** adsorbed on the TiO_2 surface.

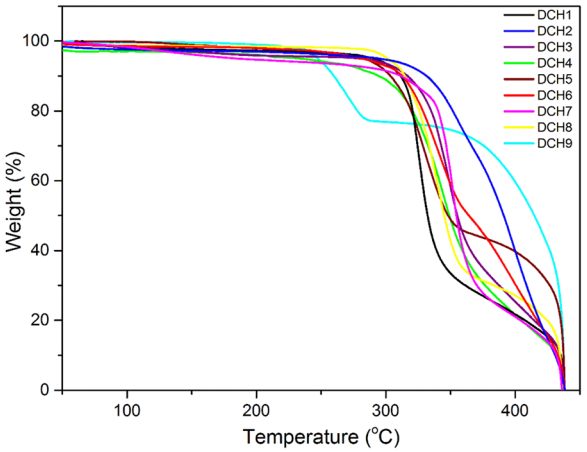

Fig. 6 TGA thermograms of **DCH$_{1-9}$** determined at a heating rate of 10 °C min^{-1} under a nitrogen atmosphere.

To further understand the light-harvesting capabilities of the synthesized dyes in DSSC fabrication, a separate experiment was conducted in which the dyes were adsorbed onto the TiO_2 surface, and the corresponding UV-vis spectra were recorded. Fig. 5 shows the absorption spectra of the **DCH$_{1-9}$** dyes adsorbed on TiO_2 films. The spectra reveal that all dyes exhibited broader absorption bands compared to their peaks in the solution state. This broadening and the observed bathochromic shift (redshift) are attributed to the interaction between the anchoring groups of the dye molecules and titanium ions on the electrode surface, along with the delocalization of the dye molecules, which lowers the overall energy of the π* orbital.[55] Among all the dyes, **DCH$_2$** showed the most significant redshift over an extended region, suggesting a strong tendency to form J-aggregates on the TiO_2 surface. This is largely due to the close interaction between the carboxylic anchor groups and Ti^{4+} ions of the semiconductor. Rhodanine-3-acetic acid contains both a carboxyl group (–COOH) and a thiazolidine ring, allowing for strong binding interactions with the TiO_2 surface, particularly through stable covalent bonding between the carboxyl group and titanium atoms (Ti^{4+}), ensuring efficient attachment of the dye to the semiconductor.[33] Furthermore, the rigid structures of **DCH$_2$** and **HD-2** help to maintain the dye orientation on the TiO_2 surface, improving the electron injection efficiency and preventing dye desorption under prolonged illumination. Therefore, the **DCH$_2$** dye can be considered a promising candidate for light-harvesting applications due to its strong anchoring capabilities.

Thermal properties

The thermal properties of the dyes **DCH$_{1-9}$** were investigated by differential scanning calorimetry (DSC) and thermogravimetric analysis (TGA) under nitrogen atmosphere with a heating rate of 10 °C min^{-1}. The TGA and DSC plots of dyes **DCH$_{1-9}$** are shown in Fig. 6 and Fig. S45 (ESI†), respectively, and the corresponding thermal data are tabulated in Table 2. All the synthesized dyes exhibit satisfactory thermal stability with high thermal decomposition (T_d) temperatures at 315 °C (**DCH$_1$**), 340 °C (**DCH$_2$**), 326 °C (**DCH$_3$**), 302 °C (**DCH$_4$**), 307 °C (**DCH$_5$**), 318 °C (**DCH$_6$**), 336 °C (**DCH$_7$**), 310 °C (**DCH$_8$**), and 258 °C (**DCH$_9$**). The melting temperature ™ of dyes **DCH$_{1-9}$** was found to be higher than 200 °C. Among all, the dye **DCH$_2$** bear rhodaminenine-3-acetic acid as an anchoring group shows higher thermal stability, making it a more relevant material for solar cell applications. Thus, because of their promising high thermal property, their application as sensitizer/co-sensitizer in DSSC would impart enhanced stability to the fabricated devices.

Electrochemical characterization

The feasibility of key thermodynamic processes in the solar cell, such as active electron injection from the excited state of the dye to the conduction band (CB) of the TiO_2 photoanode, and dye regeneration by suppressing the charge recombination between the oxidized dye molecule and the TiO_2 CB, can be effectively analyzed using cyclic voltammetry (CV). The electrochemical properties of **DCH$_{1-9}$** were measured using a conventional three-electrode system, where Ag/AgCl, glassy carbon, and a platinum plate served as the reference, working, and counter electrodes, respectively.[32,65] Tetra *n*-butyl ammonium hexafluorophosphate was used as the supporting electrolyte in acetonitrile at a scan rate of 100 mV s^{-1}. The resulting voltammograms of **DCH$_{1-9}$** are shown in Fig. S46 (ESI†). From the experimental data, the highest occupied molecular orbital/ground-state oxidation potential (HOMO/GSOP) and lowest unoccupied molecular orbital/excited state oxidation potential (LUMO/ESOP) values were calculated from the onset oxidation potential of the oxidation peak, and these values are presented in Table 3. The energy level diagram of **DCH$_{1-9}$** is depicted in Fig. 7. The GSOP and ESOP values were converted from volts (V) to electron volts (eV) relative to NHE using eqn (1) and (2).[11,63]

$$\text{GSOP} = [E^{\text{oxd}}_{\text{onset}} + 4.7\ \text{eV}] \quad (1)$$

$$\text{ESOP} = [\text{GSOP} - E_{0-0}]\ \text{eV} \quad (2)$$

The experimental GSOP/HOMO values of the dyes **DCH$_{1-9}$** were found to be −5.21 (**DCH$_1$**), −5.23 (**DCH$_2$**), −5.27 (**DCH$_3$**),

 This journal is © The Royal Society of Chemistry 2025

Open Access Article. Published on 19 1404. Downloaded on 20/11/1404 12:55:10 ..
This article is licensed under a Creative Commons Attribution 3.0 Unported Licence.

Table 3 Electrochemical characterization data of the dyes **DCH$_{1-9}$**

Compound	E_{OX}[a] (V *vs.* NHE)	$E^{\#}_{OX}$[a] (V *vs.* NHE)	HOMO[b] (eV)	LUMO[b] (eV)	ΔG_{inj} (eV)	ΔG_{rec} (eV)	ΔG_{reg} (eV)
DCH$_1$	0.51	−2.23	−5.21	−2.47	1.73	−1.01	−0.11
DCH$_2$	0.53	−2.17	−5.23	−2.53	−1.67	−1.03	−0.13
DCH$_3$	0.57	−2.08	−5.27	−2.62	−1.58	−1.07	−0.17
DCH$_4$	0.58	−2.06	−5.28	−2.64	−1.56	−1.08	−0.18
DCH$_5$	0.76	−1.80	−5.46	−2.90	−1.30	−1.26	−0.36
DCH$_6$	0.77	−1.68	−5.47	3.01	−1.19	−1.27	−0.37
DCH$_7$	0.525	−2.20	−5.23	−2.49	−1.70	−1.02	−0.12
DCH$_8$	0.66	−1.96	−5.36	−2.74	−1.46	−1.16	−0.26
DCH$_9$	0.67	−1.94	−5.37	−2.76	−1.44	−1.17	−0.27

[a] The E^* values were formulated by, $E^{\#}_{OX} = E_{OX} - E_{0-0}$. [b] All the potentials were obtained during cyclic voltammetric investigations in 0.1 M Bu_4NPF_6 in DMF, and platinum electrode diameter: 1 mm, sweep rate: 100 mV s^{-1}.

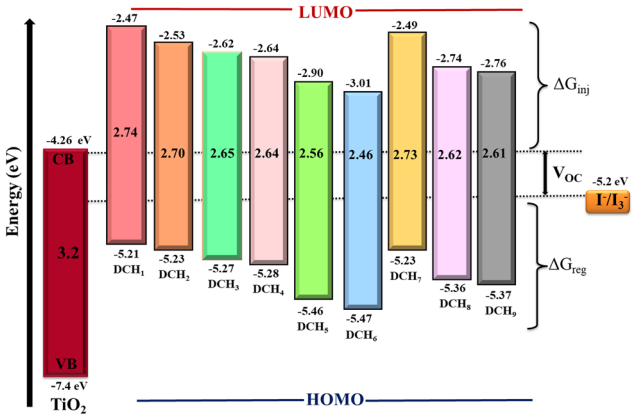

Fig. 7 Molecular energy level diagram showing the experimental HOMO, LUMO, and bandgap values of **DCH$_{1-9}$**.

−5.28 (**DCH$_4$**), −5.46 (**DCH$_5$**), −5.47 (**DCH$_6$**), −5.23 (**DCH$_7$**), −5.36 (**DCH$_8$**), −5.37 (**DCH$_9$**) respectively, which are much lower than that of the redox potential of the I_3^-/I^- electrolyte system (−5.2 eV), favouring quick ground-state regeneration process. Among all, the dye **DCH$_1$** has the highest positive potential, stabilizing the dye molecule in its oxidized state and facilitating effective electron injection, which is necessary for the affirmative transition of charges through the energy conversion cycle. The reason may be due to the presence of superior electron-donating carbazole twin moieties and a strong cyanoacetic acid as an anchoring unit. Cyanoacetic acid generally exhibits a higher oxidation potential due to its strong electron-withdrawing cyano (–CN) group.[66] This higher potential can enhance electron injection from the dye to the TiO_2 conduction band, making it favorable for applications that require strong electron transfer. Furthermore, the experimental ESOP/LUMO values of the dyes **DCH$_{1-9}$** are found to be −2.47 (**DCH$_1$**), −2.53 (**DCH$_2$**), −2.62 (**DCH$_3$**), −2.64 (**DCH$_4$**), −2.90 (**DCH$_5$**), −3.01 (**DCH$_6$**), −2.49 (**DCH$_7$**), −2.74 (**DCH$_8$**), −2.76 (**DCH$_9$**), respectively, which are greater than the potential of the CB of the TiO_2 semiconductor (−4.2 eV), facilitating enhanced electron injection phenomenon. Among all the dyes, **DCH$_1$** has ideal HOMO and LUMO levels, facilitating an adequate thermodynamic driving force that is mandatory for the affirmative transition of changes throughout the energy cycle.

To investigate the different thermodynamic pathways, such as dye injection, recombination, and regeneration processes of **DCH$_{1-9}$**, the driving forces, *viz.*, free energies (ΔG_{inj}, ΔG_{rec}, and ΔG_{reg}) were estimated using eqn (3) through eqn (5), and the corresponding data are given in Table 3.

$$\Delta G_{inj} = E^*_{OX} - E_{CB} \quad (3)$$

$$\Delta G_{rec} = E_{CB} - E_{OX} \quad (4)$$

$$\Delta G_{reg} = E_{I_3^-/I^-} - E_{OX} \quad (5)$$

From the calculated data, it is clear that all the free energy values are negative, describing the thermodynamical feasibility of the aforesaid processes. The ΔG_{inj} (free energy for electron injection from LUMO to the conduction band of TiO_2) values were calculated from the difference between the LUMO level of the dyes and semiconductor, and are in the following order: **DCH$_1$** (−1.73 eV) > **DCH$_7$** (−1.70 eV) > **DCH$_2$** (−1.67 eV) > **DCH$_3$** (−1.58 eV) > **DCH$_4$** (−1.56 eV) > **DCH$_8$** (−1.46 eV) > **DCH$_9$** (−1.44 eV) > **DCH$_5$** (−1.30 eV) > **DCH$_6$** (−1.19 eV). It is worth noting that the dye **DCH$_1$** has the highest value of ΔG_{inj}, indicating efficient electron injection to the CB of TiO_2. The reason may be due to the presence of the strong electron-withdrawing nature of cyanoacetic acid, along with the increased carbazole donor strength. Its D–A strength thermodynamically drags electrons from the LUMO energy level, and injects them to the CB edge of the TiO_2 and HOMO energy level towards the redox electrolyte. The calculated ΔG_{rec} values of dyes **DCH$_{1-9}$** are as follows: −1.01 (**DCH$_1$**), −1.03 (**DCH$_2$**), −1.07 (**DCH$_3$**), −1.08 (**DCH$_4$**), −1.26 (**DCH$_5$**), −1.27 (**DCH$_6$**), −1.02 (**DCH$_7$**), −1.16 (**DCH$_8$**), −1.17 (**DCH$_9$**), respectively. Similarly, the ΔG_{reg} values of dyes **DCH$_{1-9}$** are found to be: −0.11 (**DCH$_1$**), −0.13 (**DCH$_2$**), −0.17 (**DCH$_3$**), −0.18 (**DCH$_4$**), −0.36 (**DCH$_5$**), −0.37 (**DCH$_6$**), −0.12 (**DCH$_7$**), −0.26 (**DCH$_8$**), −0.27 (**DCH$_9$**). From the results, it is clear that the dye **DCH$_1$** comprising two carbazole donor moieties and the strong electron acceptor cyanoacetic acid shows the highest negative free energy for the electron regeneration process to resist its recombination between electron injection and photo-oxidized dye molecules, making the ΔG_{rec} and ΔG_{reg} processes energetically favourable. The presence of a long linear alkyl chain functions as an insulating

Open Access Article. Published on 19 1404. Downloaded on 20/11/1404 12:55:10 ..
This article is licensed under a Creative Commons Attribution 3.0 Unported Licence.

barrier, thereby minimizing interfacial charge recombination in the DSSCs. Conclusively, all the dyes fulfil basic requirements by providing nearly the same negative values of free energy changes, demonstrating a good balance in the thermodynamic properties of various photo-electronic processes.

Photovoltaic and electrochemical impedance studies

To gain a deeper understanding of the structure–performance relationships, anchor-dependent surface chemistry, cell electrochemistry, and device photophysics, the photoelectrochemical characteristics of DSSCs sensitized with **DCH$_{1-9}$** were evaluated, following the procedure outlined in the ESI.† For accurate comparison, all devices were fabricated and characterized under identical conditions.[55] The photocurrent density *versus* voltage (*J*–*V*) curves of the DSSCs, sensitized with **DCH$_{1-9}$** and using an I^-/I_3^- liquid electrolyte in acetonitrile medium under standard AM 1.5G (100 mW cm^{-2}) irradiation, are presented in Fig. 8(a), with the corresponding device performance data summarized in Table 4. The photoelectrochemical summary of dyes with similar molecular designs along with their efficiencies is presented in Table S1 (ESI†). To prevent overestimation of current due to multiple irradiations, current–voltage measurements were performed on all fabricated devices using a black metal mask with an active area of 0.18 cm^2. The overall power conversion efficiency (PCE) was calculated using key parameters derived from experimental data for the **DCH$_{1-9}$** sensitizers, including incident light power (Pin), short-circuit photocurrent (J_{SC}), open-circuit voltage (V_{OC}), and fill factor (FF), as outlined in eqn (6).[66,67]

$$\mathrm{PCE}(\eta) = \frac{J_{SC} \times V_{OC} \times \mathrm{FF}}{P_{in}} \quad (6)$$

Among all the dyes, the device fabricated using dye **DCH$_1$** and **DCH$_2$** as the sensitizer exhibited the highest PCE of 2.45% (J_{SC} = 6.47 mA cm^{-2}, V_{OC} = 0.64 V, and FF = 58.69%) and 2.23% (J_{SC} = 5.92 mA cm^{-2}, V_{OC} = 0.57 V, and FF = 66%), respectively. Meanwhile, the dyes **DCH$_{3-9}$** displayed relatively lower PCE (<1%) under the same measuring conditions. The superior performance of **DCH$_{1-2}$** compared to the relatively lower PCE observed in others can be attributed to several key factors related to the molecular structure, charge-transfer dynamics, dye-TiO_2 interactions, charge recombination, energy level mismatch, and inefficient light absorption properties.[68] The molecular structures of barbituric acid (BA) and its derivatives as anchoring groups play a crucial role in determining their electronic properties, anchoring capability, and charge-transfer characteristics.[69] The BA anchoring group in **DCH$_5$** contains a triketone (–C═O) electron-withdrawing core, which promotes intramolecular charge transfer (ICT) and enables strong hydrogen bonding and coordination interactions with TiO_2.[70] This results in increased dye loading and better electron injection efficiency, which eventually leads to increased J_{SC} through enhanced electron transfer into the conduction band. However, its strong interaction with the electrolyte also accelerates charge recombination at the TiO_2/electrolyte interface, increasing series resistance and ultimately leading to a lower fill factor (FF). In contrast, **DCH$_6$** with 1,3-diethyl-2-thiobarbituric acid substitutes one oxygen (O) atom with sulfur (–C═S) and contains bulky diethyl (–C_2H_5) groups.[69,71] It changes the electronic density and orbital overlap, induces steric hindrance, and decreases the dye surface coverage and electron injection efficiency, despite its broader light absorption. These structural changes significantly affect the overall photovoltaic performance, highlighting the critical role of the anchoring group selection in designing dye-sensitized solar cells (DSSCs).

Table 4 The photoelectrochemical parameters of the fabricated DSSCs using **DCH$_{1-9}$**

Sensitizer	J_{SC} (mA cm^{-2})	V_{OC} (V)	FF (%)	PCE (%)	τ_{eff} (ms)
DCH$_1$	6.472	0.643	58.69	2.45	0.45
DCH$_2$	5.929	0.578	66.08	2.23	0.44
DCH$_3$	1.179	0.494	55.49	0.32	0.43
DCH$_4$	0.335	0.536	55.01	0.09	0.30
DCH$_5$	2.500	0.165	28.47	0.11	0.43
DCH$_6$	0.609	0.539	63.19	0.20	0.41
DCH$_7$	1.270	0.569	65.03	0.47	0.43
DCH$_8$	0.495	0.548	53.76	0.14	0.40
DCH$_9$	0.320	0.504	45.37	0.07	0.31

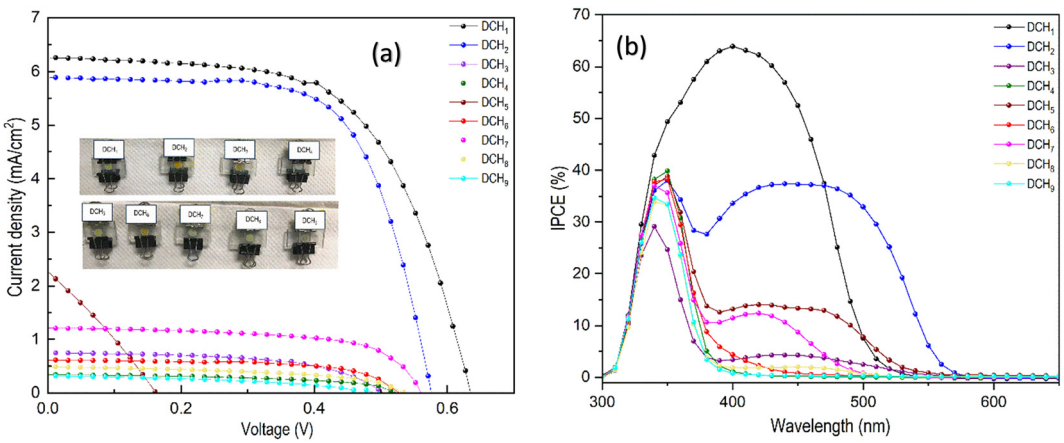

Fig. 8 (a) Current density–voltage plots of DSSCs sensitized with **DCH$_{1-9}$**, (b) IPCE spectra of DSSCs sensitized with dyes **DCH$_{1-9}$**.

 This journal is © The Royal Society of Chemistry 2025

Open Access Article. Published on 19 1404. Downloaded on 20/11/1404 12:55:10 ..
This article is licensed under a Creative Commons Attribution 3.0 Unported Licence.

Furthermore, BA-based dye **DCH$_5$** exhibits lower V_{OC} due to the enhanced charge recombination at the electrolyte interface. The lowered open-circuit voltage and high effective electron lifetime (τ_{eff}) of barbituric acid, compared with rhodanine and thiazolidinedione-based dyes **DCH$_3$** and **DCH$_7$**, can be attributed to the critical features of the dye-sensitized solar cell (DSSC) photophysics and interfacial charge behavior, despite these compounds having similar τ_{eff} values and different V_{OC}. The robust dipole moment manifested by barbituric acid due to its electron-withdrawing ureido (–NHCO) groups induces a downward shift in the conduction band (CB) of TiO_2. This displacement lowers V_{OC} despite having a larger τ_{eff}. In addition, the greater dye-electrolyte interaction in BA-based devices enhances the charge recombination between the injected electrons in TiO_2 and tri-iodide (I_3^-) in the electrolyte, leading to increased electron loss. This reaction lowers the electron density in TiO_2, decreasing the quasi-Fermi level and hence lowering V_{OC}. Although **DCH$_5$** obtains larger J_{SC}, its lower V_{OC} and larger recombination rates decrease the overall power conversion efficiency (PCE).[72] The same pattern appears when **DCH$_4$**, with more rapid electron back-transfer to I_3^-, leads to greater charge losses, detrimentally affecting the charge collection efficiency and further decreasing the performance of DSSCs. Conversely, thiazolidinedione and rhodamine are not affected by a substantial dipole-induced shift in the conduction band, and are thus able to retain a higher conduction band edge, resulting in an elevated V_{OC}. Moreover, although barbituric acid can display a larger τ_{eff} caused by surface passivation effects, it also can cause decreased charge collection and further decreases V_{OC}. Another important issue relates to the electrolyte interaction since barbituric acid also shows strong interaction with the iodide/tri-iodide redox couple, and thus causes high electron back transfer. However, rhodamine and thiazolidinedione show stronger interfacial energy barriers, thus lowering the recombination of the charge at the TiO_2/electrolyte interface, which in turn helps retain a higher V_{OC}.

The poor efficiency of **DCH$_8$** and **DCH$_9$** is mainly due to their weaker binding affinity to TiO_2, leading to lower surface coverage and suboptimal electron injection efficiency. The oxindole anchoring group in **DCH$_8$**, due to its rigid fused ring structure and lactam (–C═O) functionality, has a lower driving force for electron transfer and weaker electronic coupling with TiO_2, resulting in poor charge separation and higher recombination rates.[73] While the oxindole group can form hydrogen bonds, it lacks the strong covalent interactions that the carboxyl-based anchoring groups in **DCH$_1$** and **DCH$_2$** provide, leading to weaker dye adsorption and higher dye desorption over time, negatively impacting the device performance. Similarly, the 4-nitrophenyl acetonitrile anchoring group in **DCH$_9$**, despite containing a nitro ($-NO_2$) electron-withdrawing group, exhibits poor energy level alignment, which can increase the charge recombination losses and reduce V_{OC}. Overall, the weaker electron-withdrawing ability, inefficient charge injection, poor dye anchoring, and increased recombination losses contribute to the lower efficiency of **DCH$_8$** and **DCH$_9$** compared to the cyanoacetic acid and rhodanine-3-acetic acid derivatives.

The superior PCE values of **DCH$_{1–2}$** can be attributed to the efficient electron extraction from the twin carbazole donor units and strong electron injection into the TiO_2 conduction band, enabled by the electron-withdrawing cyanoacetic acid and rhodanine-3-acetic acid anchoring groups. Additionally, the alkyl chain reduces the surface hydration on the semiconductor. **DCH$_{1–2}$** achieves the highest J_{SC} due to the higher dye loading on the TiO_2 surface, driven by the strong binding capacity of the anchoring groups, leading to improved charge collection and favorable electron injection (ΔG_{inj}). In contrast, the lower J_{SC} of **DCH$_{3–9}$** is due to the weaker adsorption of the anchoring units, impairing the light-harvesting efficiency. The higher V_{OC} of **DCH$_{1–2}$** is attributed to the *n*-hexyl alkyl chain, which reduces dye aggregation and minimizes interfacial recombination. Most dyes exhibit FF values between 50–65%, except for **DCH$_5$**, where the increased interfacial recombination, likely caused by the higher series and lower shunt resistance, reduces the FF. Overall, cyanoacetic acid and rhodanine-3-acetic acid are superior anchoring groups due to their strong electron-withdrawing properties, better TiO_2 binding, enhanced light absorption, and efficient charge transfer, contributing to improved device efficiency.

In general, the photovoltaic cell performance of DSSCs is notably based on the interfacial charge recombination and carrier transport processes, electron lifetime (τ_{eff}), and incident photon-to-current conversion efficiency (IPCE) of the fabricated devices.[55] Fig. 8(b) displays the IPCE spectra as a function of wavelength for the DSSCs based on the nine new dyes **DCH$_{1–9}$** as sensitizers, and the corresponding values are calculated using eqn (7).

$$\mathrm{IPCE} = \mathrm{LHE} \times \phi_{inj} \times \phi_{reg} \times \eta_{cc} \quad (7)$$

Where LHE represents the light-harvesting efficiency of DSSCs (LHE = $1–10^{-A}$, A is the absorbance of the photoanode, which is same as oscillator strength), and ϕ_{inj}, ϕ_{reg}, and η_{cc} are the electron injection, electron regeneration, and charge collection efficiencies, respectively.[65] The IPCE was measured by recording the photocurrent at various monochromatic excitations, and the resulting spectra aligned with the absorption spectra of the photocathodes (Fig. 4). As shown in Fig. 8(b), **DCH$_1$** achieved an IPCE of 65% over a broad spectral range from 300–600 nm, while **DCH$_{2–9}$** displayed maxima below 50%. Among all, **DCH$_1$** displayed higher IPCE in the longer wavelength region than others. This is attributed to its strong electron-withdrawing anchoring unit, efficient TiO_2 binding, enhanced light absorption, higher dye loading, and improved charge transfer. In conclusion, **DCH$_1$**, with cyanoacetic acid as a strong acceptor and a linear hexyl chain, promotes better electron injection, reduced recombination, and improved device performance.

Electrochemical impedance spectroscopy (EIS) has been performed to investigate the interfacial charge recombination, carrier transport, and their influence on the open-circuit voltage (V_{OC}) of the fabricated devices, which directly affects the overall performance of DSSCs.[74–77] The EIS spectra for **DCH$_{1–9}$** were recorded over a frequency range of 100–200 kHz at 298 K

Open Access Article. Published on 19 1404. Downloaded on 20/11/1404 12:55:10 ..
This article is licensed under a Creative Commons Attribution 3.0 Unported Licence.

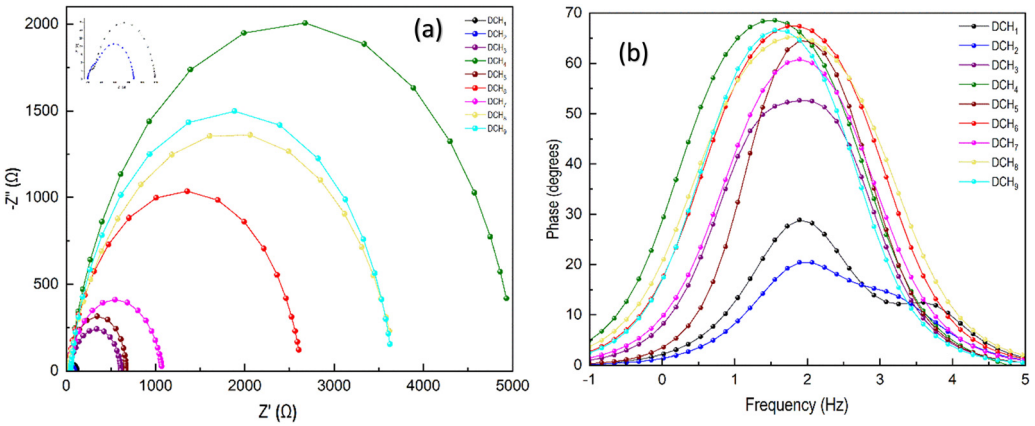

Fig. 9 EIS spectra of devices sensitized with dyes **DCH$_{1-9}$**: (a) Nyquist plots, (b) Bode phase plots.

under AM 1.5 G illumination, with a forward bias set at V_{OC} (bias voltage applied for **DCH$_{1-9}$** are −0.64 V, −0.57 V, −0.49 V, −0.53 V, −0.16 V, −0.53 V, −0.56 V, −0.54 V, −0.5 V respectively) and a 10 mV amplitude. Fig. 9(a) shows the Nyquist plots at open-circuit voltage, and the equivalent circuit for the data fitting is presented in Fig. S47 (ESI†). In these plots, the series resistance (R_S) is identified by the higher frequency intercept on the real axis, while the high-frequency region represents the charge-transport resistance (R_{Pt}) and interface capacitance (C_{Pt}) at the counter electrode/redox electrolyte interface. The low-frequency region corresponds to the chemical capacitance (C_μ) and charge recombination resistance (R_{CT}) at the TiO_2/dye/electrolyte interface. For sensitized devices, C_μ and C_{Pt} are replaced by a constant phase element (CPE) in the equivalent circuit. A higher R_{Pt} value indicates a more difficult electron injection from TiO_2 to the redox electrolyte, suggesting suppressed back recombination and improved V_{OC}. The Nyquist plots display a distinct semicircle in the middle-frequency range, corresponding to charge-transfer resistance (R_{CT}) at the TiO_2/dye/electrolyte interface, which reflects electron transfer through TiO_2 and back electron transfer to the I^-/I_3^- electrolyte.[55]

In EIS analysis, the area of the semicircle is also equally important. Larger radii correspond to Nernst impedance, *i.e.*, R_r (dark reaction impedance) ≫ R_d (diffusion impedance). Normally, Nernst impedance relates to the diffusion of redox species (like the I^-/I_3^- couple) in the electrolyte. If diffusion is slow, this impedance dominates and results in a larger semicircle, particularly in the low-frequency region of the Nyquist plot.[33] A larger semicircle indicates higher Nernst impedance, signifying the poor diffusion of the redox species in the electrolyte, which limits the regeneration of the dye and lowers the current generation. Gerischer impedance describes the coupling between the charge transfer at the TiO_2/dye/electrolyte interface and diffusion of the redox species. Instead of a simple semicircle, Gerischer's impedance often appears as a sloped or smaller semicircle in the Nyquist plot, indicating that both charge transfer and diffusion processes are occurring simultaneously.[78,79] A smaller semicircle in this region means that electron recombination is less prominent, which leads to better diffusion, allowing for faster redox reactions and more efficient dye regeneration, better charge separation, and longer electron lifetimes, improving both the short-circuit current (J_{SC}) and V_{OC}.[66] From Fig. 11(a), it is evident that **DCH$_{3-9}$** follow the Nernst impedance, whereas **DCH$_{1-2}$** show the Gerischer impedance. In the present study, the radius of the semicircle obtained for **DCH$_{1-9}$** is increasing in the order, **DCH$_{1-2}$** < **DCH$_{3-9}$**, indicating the electron recombination resistance decreases in the order of **DCH$_{1-2}$** > **DCH$_{3-9}$** since the type of impedance involved is Greischer impedance, which is further aligned with the V_{OC} values of the dyes. Hence, dye **DCH$_1$** achieved the highest V_{OC} value due to the increased electron injection, high resistance towards the recombination rate, and thus the highest PCE.

Furthermore, the Bode angle phase plots and Bode amplitude plots obtained from fabricated cells using the **DCH$_{1-9}$** sensitizers are depicted in Fig. 9(b). The Bode phase plots were used to calculate the effective lifetime (τ_{eff}) of the electron in CB of the semiconductor using eqn (8), and the corresponding data are summarized in Table 4.

$$\tau_{eff} = \frac{1}{2\pi f_{max}} \quad (8)$$

where, the value of f_{max} is obtained from the frequency of the corresponding midpoint in the Bode phase plot.[57] The higher value of τ_{eff} indicates a lower electron recombination rate and hence facilitates improved V_{OC} of the device. From the results, it is evident that dyes **DCH$_{1-2}$** carrying cyanoacetic acid and rhodamine-3-acetic acid display higher electron lifetime than that of **DCH$_{3-9}$**, resulting in a lower recombination process. Moreover, a longer electron lifetime indicates reduced recombination rates, meaning electrons remain in the TiO_2 conduction band for a longer time. This typically results in higher open-circuit voltage (V_{OC}) and overall better device performance. The longer τ_{eff} often results from better passivation of the TiO_2 surface, improved dye binding, or reduced interaction between the injected electrons and the electrolyte. Conclusively, the detailed EIS studies revealed the synergetic effect of different

 This journal is © The Royal Society of Chemistry 2025

Open Access Article. Published on 19 1404. Downloaded on 20/11/1404 12:55:10 ..
This article is licensed under a Creative Commons Attribution 3.0 Unported Licence.

anchoring units in the fine-tuning of the charge-transport resistance, recombination resistance and electron lifetime.

Anchoring studies of dyes DCH_{1-9} on the TiO_2 surface: FTIR analysis

To investigate the anchoring behavior of dyes **DCH_{1-9}** on the TiO_2 surface, FTIR spectral analysis was performed on both free and adsorbed dyes (Fig. S47, ESI†). The binding mechanisms of the dye anchoring groups were examined using Deacon–Phillips empirical rules, which relate the difference between the symmetric and asymmetric bond stretching frequencies ($\Delta\nu$). Three binding modes were identified: monodentate ($\Delta\nu_{ads} > \Delta\nu_{solid}$), bidentate ($\Delta\nu_{ads}s < \Delta\nu_{solid}$), and chelating ($\Delta\nu_{ads} \ll \Delta\nu_{solid}$).[55] Their FTIR spectra (Fig. S46, ESI†) indicated that **DCH_1** adsorbs on TiO_2 *via* a bidentate bridging mode, confirming deprotonation and involvement of the carboxylic acid group. Interestingly, the cyano group has not participated in the dye adsorption mechanism, as its peak position remains unchanged in both free and adsorbed states. Similar trends were observed for dyes **DCH_{2-9}**.

Co-sensitization studies

The photovoltaic properties of the DSSCs fabricated using **DCH_{1-9}** dyes as co-sensitizers, along with a ruthenium-based dye **HD-2**, are manifested in Fig. 10(a), and the pertaining photovoltaic parameters are listed in Table 5. The detailed fabrication procedure is given in the ESI.† Interestingly, the co-sensitizer **DCH_2** (*i.e.*, **DCH_2** + **HD-2**) shows a higher PCE of 8.82% than the **HD-2** dye alone (η = 6.79%). Several factors impact the overall cell performance, including the TiO_2 thickness, the solvent used, and the added additives. Different solvents were tested for dyeing the TiO_2 electrodes, as dyes can interact differently with solvents, affecting their interaction with the semiconductor surface. Dyeing solutions also included varying amounts of chenodeoxycholic acid (CDCA), an additive that reduces dye aggregation on TiO_2, decreases recombination between TiO_2 electrons and the electrolyte, and positively shifts the TiO_2 surface potential, improving the V_{OC}. Optimal results were achieved with alcoholic solutions containing 0.2 mM dye and 20 mM CDCA. The incorporation of CDCA has a positive impact in increasing V_{OC}, suggesting a positive shift in the TiO_2 vacuum level and its conduction band edge.

Table 5 The photovoltaic performance data of devices sensitized with **HD-2** alone and co-sensitized using **DCH_{1-9}**

Sensitizer/ co-sensitizer		CDCA (mM)	J_{SC} (mA cm^{-2})	V_{OC} (V)	FF (%)	PCE (%)	τ_{eff} (ms)
HD-2 (mM)	Dyes (0.2 mM)						
0.2	—	20	15.52	0.68	64.10	6.79	0.316
0.2	**DCH_1**	20	19.43	0.69	60.73	8.15	0.373
0.2	**DCH_2**	**20**	**20.72**	**0.66**	**63.92**	**8.82**	**0.506**
0.2	**DCH_3**	20	19.05	0.64	64.67	7.90	0.486
0.2	**DCH_4**	20	18.33	0.67	64.87	8.01	0.483
0.2	**DCH_5**	20	17.00	0.68	68.84	8.01	0.427
0.2	**DCH_6**	20	20.64	0.63	52.94	6.96	0.373
0.2	**DCH_7**	20	22.06	0.63	57.29	7.98	0.377
0.2	**DCH_8**	20	19.00	0.69	64.39	8.54	0.493
0.2	**DCH_9**	20	21.92	0.66	58.35	8.52	0.499

It is evident from the result that the device fabricated using **DCH_2** as a co-sensitizer shows excellent performance with more than a 25% increment compared to that of the device sensitized using the **HD-2** dye alone. Furthermore, there is an increase in the V_{OC} values of devices co-sensitized with dyes **DCH_{1-9}**, suggesting the charge recombination of photoinjected electrons caused by ruthenium dye aggregation is significantly minimized. Specifically, the bulky ruthenium molecules of the **HD-2** dye do not adsorb efficiently on the surface of the TiO_2 nanoparticles, leading to larger gaps between the adsorbed dye molecules. These voids can be effectively filled by small metal-free organic molecules acting as co-sensitizers, which help create a more uniform coverage and increase the surface area for light harvesting in the visible region.[45] Finally, the uniform adsorption of **DCH_{1-9}** on the TiO_2 surface drastically suppresses the dye aggregation of **HD-2**, as well as the back-reaction of the I_3^-/I^- on the semiconductor surface. The enhanced J_{SC} and FF values of **DCH_2** may be attributed to its

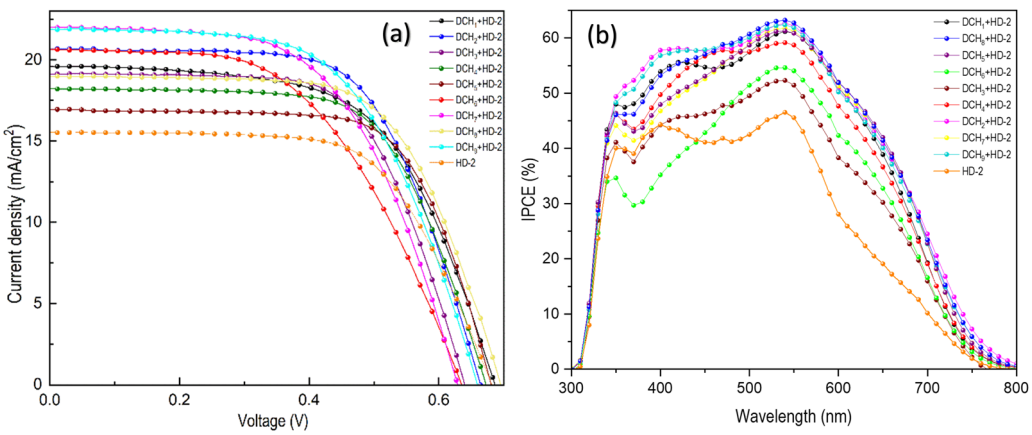

Fig. 10 (a) Current density–voltage plots of DSSCs sensitized with **HD-2** alone and co-sensitized using **DCH_{1-9}**. (b) IPCE spectra of DSSCs sensitized with **HD-2** alone and co-sensitized using **DCH_{1-9}**.

Open Access Article. Published on 19 1404. Downloaded on 20/11/1404 12:55:10 ..
This article is licensed under a Creative Commons Attribution 3.0 Unported Licence.

strong intermolecular interactions causing efficient electron injection and charge transport towards the electrodes. Furthermore, the poor device performance in the case of **HD-2** is ascribed to reduced electron injection, which is because of the inhomogeneous dye loading on the TiO_2 surface.

IPCE spectra of the fabricated devices using dyes **DCH$_{1-9}$** as co-sensitizers, along with reference dye **HD-2**, are shown in Fig. 10(b). The obtained spectrum of the device comprising **DCH$_{1-9}$** + **HD-2** showed an intense external quantum efficiency (EQE) in the broad spectrum of 300–800 nm with a maximum value at 500–600 nm compared to the reference dye **HD-2** (45% at 540 nm). The integrated J_{SC} values from the IPCE spectra of DSSCs sensitized with **HD-2** alone and co-sensitized with **DCH$_{1-9}$** are presented in Fig. S48 (ESI†). The calculated integrated J_{SC} values of **HD-2** and co-sensitized using **DCH$_{1-9}$** were found to be 15.02 mA cm^{-2} (**HD-2**), 19.52 mA cm^{-2} (**DCH$_1$**), 20.12 mA cm^{-2} (**DCH$_2$**), 19.50 mA cm^{-2} (**DCH$_3$**), 18.23 mA cm^{-2} (**DCH$_4$**), 17.46 mA cm^{-2} (**DCH$_5$**), 19.96 mA cm^{-2} (**DCH$_6$**), 21.86 mA cm^{-2} (**DCH$_7$**), 19.02 mA cm^{-2} (**DCH$_8$**), and 21.18 mA cm^{-2} (**DCH$_9$**), respectively (Fig. S48, ESI†). The measured J_{SC} values of all devices are in good agreement with the integrated current density values as estimated from the IPCE spectra of the co-sensitized devices, indicating that the emission of our solar simulator is in agreement with the spectrum of the standard air mass 1.5 illumination. The results obtained from the IPCE spectra are in agreement with the current–voltage measurements. The IPCE maximum of **DCH$_1$** is 61%, **DCH$_2$** is 65%, **DCH$_3$** is 61.5%, **DCH$_4$** is 54%, **DCH$_5$** is 52%, **DCH$_6$** is 58%, **DCH$_7$** is 64%, **DCH$_8$** is 63%, and **DCH$_9$** is 63.5% at 420 nm. Among all the co-sensitizers, barbituric acid and its derivative **DCH$_{4-5}$** displayed both lower IPCE and J_{SC} values, which is due to the poor orientation of dye in between the bulky **HD-2** dye molecules, as well as enhanced spatial separation of the LUMO level of the dye occupied in the excited state from the semiconductor surface. Interestingly, dye **DCH$_2$** with rhodanine-3-acetic acid as a co-sensitizer displayed a broad IPCE response in the visible range (65% at 540 nm) and an enhanced anchoring effect on the TiO_2 surface compared to **HD-2** alone, attributing greater flexibility in binding orientations. This improvement is attributed to the increased flexibility in binding orientations. The reorientation effect of **DCH$_2$** and its ability to wrap around the Ru center of **HD-2** likely contribute to the enhanced irradiation efficiency and reduced recombination reactions.

To better understand the various electronic processes involved in energy conversion, EIS measurements were performed on devices co-sensitized with dyes **DCH$_{1-9}$**, alongside a reference device sensitized with **HD-2**, as shown in Fig. 11 and Fig. S49 (ESI†). From Fig. 11(a), it is evident that the Nyquist plots of all devices exhibit two distinct semicircles. As reported in the literature, the smaller semicircle at the higher frequency region corresponds to the charge transfer resistance at the cathode, which is directly related to the device's fill factor (FF). In contrast, the larger semicircle at the middle-frequency region represents the recombination resistance at the TiO_2/dye/electrolyte interface, which is directly linked to the open-circuit voltage (V_{OC}). From Fig. 11(a), it is apparent that the radius of the semicircle of **HD-2** is greater than that of **DCH$_2$** + **HD-2**, in accordance with the corresponding order of open-circuit voltage (Table 5) and is helpful in the suppression of dark current. Here, the diameter of the semicircles corresponds to the resistances (charge transfer and recombination). Co-sensitized systems with rhodamine-3-acetic acid anchoring group exhibited smaller semicircle diameters, especially at high frequencies, representing improved charge-transport dynamics.

Among all, dye **DCH$_2$** + **HD-2** manifested enhanced series resistance (R_S) of 28.46 Ω (Table S2, ESI†), which is higher than the others. The dye **DCH$_1$** + **HD-2**, which has a longer conjugation system, leads to a decrease in the charge transfer resistance at the TiO_2/electrolyte interface. This indicates improved electron injection and a more efficient charge-transfer process due to better dye anchoring on TiO_2. The R_{Pt} value of dye **DCH$_2$** + **HD-2** is higher, showing the uniform filling of voids in between the Ru-based **HD-2** molecules by co-sensitizer **DCH$_2$**. Among dyes **DCH$_{1-9}$**, the co-sensitizer **DCH$_2$** demonstrates enhanced J_{SC}, V_{OC}, and FF values, resulting in excellent device performance. Hence, it can be considered the best co-sensitizer for **HD-2** dye.

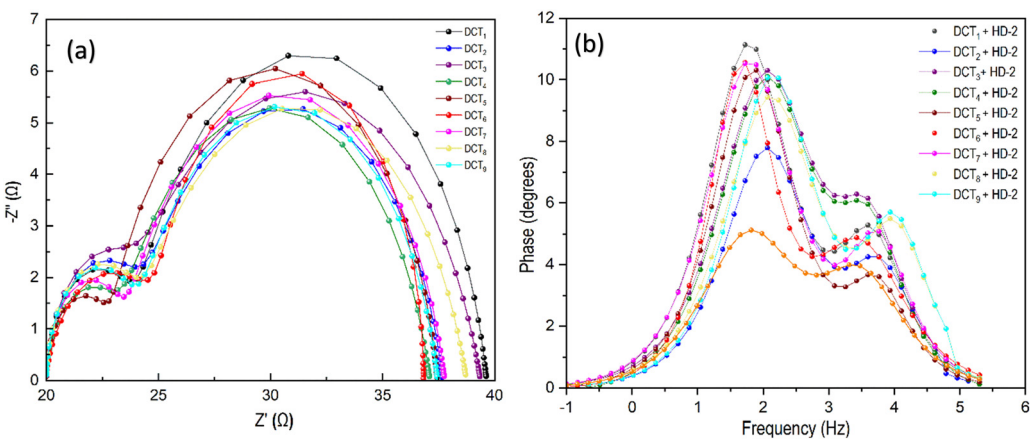

Fig. 11 EIS spectra of devices co-sensitized with **HD-2** using **DCH$_{1-9}$**: (a) Nyquist plots, (b) Bode phase plots.

 This journal is © The Royal Society of Chemistry 2025

Open Access Article. Published on 19 1404. Downloaded on 20/11/1404 12:55:10 ..
This article is licensed under a Creative Commons Attribution 3.0 Unported Licence.

Fig. 11(b) and Fig. S47 (ESI†) present the EIS Bode phase plots for co-sensitized devices using **DCH_{1-9}** and the reference dye **HD-2**. All devices exhibit two distinct peaks: the high-frequency peak corresponds to electron transfer at the Pt/electrolyte interface, while the low-frequency peak is associated with charge transfer at the TiO_2/dye/electrolyte interface.[16,64] Additionally, the electron lifetimes for all co-sensitized devices were calculated using eqn (8), with the corresponding values listed in Table 5. The electron lifetime (τ_{eff}) was derived from the low-frequency peak of the Bode phase plot, and reflects the charge recombination rate at the TiO_2/dye/electrolyte interface. The results indicate that the **DCH_2** + **HD-2** combination exhibits the longest electron lifetime. This is likely due to a reduced back reaction of injected electrons from the TiO_2 conduction band with the redox electrolyte, leading to an enhanced V_{OC} compared to other co-sensitizers and **HD-2** alone. In conclusion, the **DCH_2** dye, when used as a co-sensitizer with the ruthenium-based dye **HD-2**, effectively suppresses undesirable charge recombination, thereby improving the overall performance of the device.

Reproducibility of devices

In order to investigate the reproducibility of DSSCs, data from five devices were recorded using the same procedure (as detailed in the ESI†), ensuring consistent layer thickness across all devices. Fig. 12 illustrates the statistical distribution of the key photovoltaic parameters (J_{SC}, V_{OC}, FF, and PCE) for the tested devices. Notably, the chromophore **DCH_2** carrying rhodanine-3-acetic acid anchor co-sensitized with the ruthenium-based sensitizer **HD-2** demonstrated superior performance and reproducibility, as explained in previous sections.

Conclusion

In summary, we designed and synthesized nine novel double donor–acceptor (D–A) organic sensitizers/co-sensitizers (**DCH_{1-9}**) for dye-sensitized solar cell (DSSC) applications. These dyes feature carbazole-based twin molecules as electron donors, non-conjugated linear alkyl chains as linkers, and multiple acceptor units. The synthesis method is simple, cost-effective, and involves straightforward purification steps. We conducted comprehensive optical, thermal, electrochemical, theoretical, and photovoltaic studies to evaluate their structure–property relationship. Among the sensitizers, **DCH_1**, containing a cyanoacetic acid acceptor, exhibited the highest PCE of 2.45%. This is attributed to the strong di-anchoring capability of the anchor on the TiO_2 surface, thereby enhancing light-harvesting across the visible and near-infrared spectrum, and the favorable electron-donating and -withdrawing groups that improve the thermodynamic processes of the cell. Furthermore, co-sensitization experiments with **DCH_{1-9}** (0.2 mM) demonstrated that **DCH_2**, carrying rhodanine-3-acetic acid as an anchoring unit,

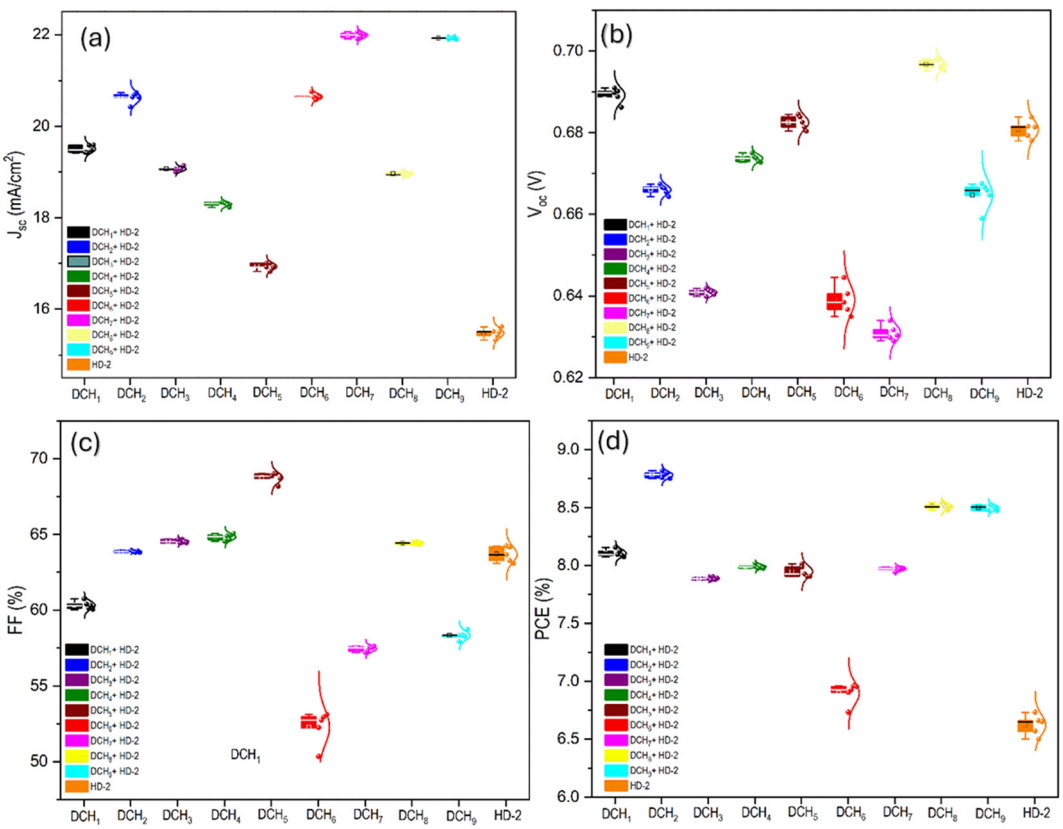

Fig. 12 Reproducibility data of devices sensitized with **HD-2** alone and co-sensitized using **DCH_{1-9}** showing the statistical distributions of various photovoltaic parameters: (a) J_{SC}, (b) V_{OC}, (c) FF, and (d) PCE.

Open Access Article. Published on 19 1404. Downloaded on 20/11/1404 12:55:10 ..
This article is licensed under a Creative Commons Attribution 3.0 Unported Licence.

achieved the highest PCE of 8.82%, with IPCE exceeding 65%, demonstrating excellent performance with more than a 25% increment compared to that of Ru-based **HD-2** dye alone (6.79%). The superior performance is due to its ability to cover voids left by the bulky molecules of **HD-2**, which reduces dye aggregation and enhances the surface area for light absorption. Thus, the present systematic study provides valuable insights into the impact of different anchoring groups on the performance of organic sensitizers/co-sensitizers in cells, offering a promising path for further enhancing the efficiency of DSSCs.

Data availability

All data supporting the findings of this study are available within the article file and its ESI.†

Conflicts of interest

The authors declare that they have no known competing financial interests or personal relationships that could have appeared to influence the work reported in this paper.

Acknowledgements

The authors are thankful to NITK, Surathkal, India, for providing the necessary laboratory facilities. The authors are also indebted to the Department of Textile Engineering, Chemistry, and Science at NCSU, Raleigh, for providing a device fabrication facility. The authors would like to express their gratitude to Dr Ahmed El-Shafei, Professor at TECS, Wilson College of Textiles, for his support and for facilitating the DSSC measurements in his laboratory.

References

1 B. O'Regan and M. Grätzel, *Nature*, 1991, **353**, 737–740.
2 M. Grätzel, *J. Photochem. Photobiol., C*, 2003, **4**, 145–153.
3 D. P. Hagberg, J.-H. Yum, H. Lee, F. De Angelis, T. Marinado, K. M. Karlsson, R. Humphry-Baker, L. Sun, A. Hagfeldt, M. Grätzel and Md. K. Nazeeruddin, *J. Am. Chem. Soc.*, 2008, **130**, 6259–6266.
4 S. Mathew, A. Yella, P. Gao, R. Humphry-Baker, B. F. E. Curchod, N. Ashari-Astani, I. Tavernelli, U. Rothlisberger, Md. K. Nazeeruddin and M. Grätzel, *Nat. Chem.*, 2014, **6**, 242–247.
5 I. M. Abdellah and A. El-Shafei, *RSC Adv.*, 2019, **10**, 610–619.
6 A. Hagfeldt, U. B. Cappel, G. Boschloo, L. Sun, L. Kloo, H. Pettersson and E. A. Gibson, in *McEvoy's Handbook of Photovoltaics*, ed. S. A. Kalogirou, Academic Press, 3rd edn, 2018, pp. 503–565.
7 A. Hagfeldt, G. Boschloo, L. Sun, L. Kloo and H. Pettersson, *Chem. Rev.*, 2010, **110**, 6595–6663.
8 P. Ferdowsi, Y. Saygili, F. Jazaeri, T. Edvinsson, J. Mokhtari, S. M. Zakeeruddin, Y. Liu, M. Grätzel and A. Hagfeldt, *ChemSusChem*, 2020, **13**, 212–220.
9 Y. Farré, F. Maschietto, J. Föhlinger, M. Wykes, A. Planchat, Y. Pellegrin, E. Blart, I. Ciofini, L. Hammarström and F. Odobel, *ChemSusChem*, 2020, **13**, 1844–1855.
10 P. Ferdowsi, Y. Saygili, F. Jazaeri, T. Edvinsson, J. Mokhtari, S. M. Zakeeruddin, Y. Liu, M. Grätzel and A. Hagfeldt, *ChemSusChem*, 2020, **13**, 212–220.
11 K. S. Keremane, A. Planchat, Y. Pellegrin, D. Jacquemin, F. Odobel and A. Vasudeva Adhikari, *ChemSusChem*, 2022, **15**, e202200520.
12 D. D. Babu, S. R. Gachumale, S. Anandan and A. V. Adhikari, *Dyes Pigm.*, 2015, **112**, 183–191.
13 G. Deogratias, O. S. Al-Qurashi, N. Wazzan, N. Seriani, T. Pogrebnaya and A. Pogrebnoi, *Struct. Chem.*, 2020, **31**, 2451–2461.
14 I. M. Abdellah, A. I. Koraiem and A. El-Shafei, *Sol. Energy*, 2019, **177**, 642–651.
15 F. Odobel, Y. Pellegrin, E. A. Gibson, A. Hagfeldt, A. L. Smeigh and L. Hammarström, *Coord. Chem. Rev.*, 2012, **256**, 2414–2423.
16 D. D. Babu, P. Naik and K. S. Keremane, *J. Mol. Liq.*, 2020, **310**, 113189.
17 H. Wang, B. Bao, X. Hu and J.-K. Fang, *Electrochim. Acta*, 2017, **250**, 278–284.
18 B. Xu, S. Wrede, A. Curtze, L. Tian, P. B. Pati, L. Kloo, Y. Wu and H. Tian, *ChemSusChem*, 2019, **12**, 3243–3248.
19 W. Zhang, X. Dai, X. Liao, X. Zang, H. Zhang, X. Yin, C. Yu, C. Ke and Y. Hong, *Sol. Energy*, 2020, **212**, 220–230.
20 M.-W. Lee, J.-Y. Kim, H.-G. Lee, H. G. Cha, D.-H. Lee and M. J. Ko, *J. Energy Chem.*, 2021, **54**, 208–216.
21 S. Mathew, A. Yella, P. Gao, R. Humphry-Baker, B. F. E. Curchod, N. Ashari-Astani, I. Tavernelli, U. Rothlisberger, Md. K. Nazeeruddin and M. Grätzel, *Nat. Chem.*, 2014, **6**, 242–247.
22 H. Imahori, T. Umeyama and S. Ito, *Acc. Chem. Res.*, 2009, **42**, 1809–1818.
23 M. R. Elmorsy, S. A. Badawy, E. Abdel-Latif, M. A. Assiri and T. E. Ali, *Dyes Pigm.*, 2023, **214**, 111206.
24 E. Tanaka, M. S. Mikhailov, N. S. Gudim, E. A. Knyazeva, L. V. Mikhalchenko, N. Robertson and O. A. Rakitin, *Mol. Syst. Des. Eng.*, 2021, **6**, 730–738.
25 J.-S. Luo, Z.-Q. Wan and C.-Y. Jia, *Chin. Chem. Lett.*, 2016, **27**, 1304–1318.
26 B.-G. Kim, K. Chung and J. Kim, *Chem. – Eur. J.*, 2013, **19**, 5220–5230.
27 K. S. Keremane and A. V. Adhikari, *Electrochem. Sci. Adv.*, 2021, **1**, e2000036.
28 Y. Hua, S. Chang, D. Huang, X. Zhou, X. Zhu, J. Zhao, T. Chen, W.-Y. Wong and W.-K. Wong, *Chem. Mater.*, 2013, **25**, 2146–2153.
29 K. S. Keremane, P. Naik and A. V. Adhikari, *J. Nano-Electron. Phys.*, 2020, **12**, 02039.
30 K. Hara, T. Sato, R. Katoh, A. Furube, Y. Ohga, A. Shinpo, S. Suga, K. Sayama, H. Sugihara and H. Arakawa, *J. Phys. Chem. B*, 2003, **107**, 597–606.
31 N. Robertson, *Angew. Chem., Int. Ed.*, 2006, **45**, 2338–2345.
32 P. Naik, K. S. Keremane, M. R. Elmorsy, A. El-Shafei and A. V. Adhikari, *Electrochem. Sci. Adv.*, 2022, **2**, e2100061.

 This journal is © The Royal Society of Chemistry 2025

Open Access Article. Published on 19 1404. Downloaded on 20/11/1404 12:55:10 ..
This article is licensed under a Creative Commons Attribution 3.0 Unported Licence.

33 P. Naik, I. M. Abdellah, M. Abdel-Shakour, R. Su, K. S. Keremane, A. El-Shafei and A. Vasudeva Adhikari, *Sol. Energy*, 2018, **174**, 999–1007.
34 M. R. Elmorsy, R. Su, A. A. Fadda, H. A. Etman, E. H. Tawfik and A. El-Shafei, *Dyes Pigm.*, 2018, **158**, 121–130.
35 L. Zhang and J. M. Cole, *J. Mater. Chem. A*, 2017, **5**, 19541–19559.
36 B. Xiao, A. Tang, J. Zhang, A. Mahmood, Z. Wei and E. Zhou, *Adv. Energy Mater.*, 2017, **7**, 1602269, DOI: **10.1002/aenm.201602269**.
37 T. Dai, Y. Meng, Z. Wang, J. Lu, Z. Zheng, M. Du, Q. Guo and E. Zhou, *J. Am. Chem. Soc.*, 2025, **147**, 4631–4642.
38 T. Dai, A. Tang, Y. Meng, C. Dong, P. Cong, J. Lu, J. Du, Y. Zhong and E. Zhou, *Angew. Chem., Int. Ed.*, 2024, **63**, e202403051, DOI: **10.1002/anie.202403051**.
39 K. Zeng, Z. Tong, L. Ma, W.-H. Zhu, W. Wu and Y. Xie, *Energy Environ. Sci.*, 2020, **13**, 1617–1657.
40 K. Zeng, Y. Chen, W.-H. Zhu, H. Tian and Y. Xie, *J. Am. Chem. Soc.*, 2020, **142**, 5154–5161.
41 J. Luo, Z. Xie, J. Zou, X. Wu, X. Gong, C. Li and Y. Xie, *Chin. Chem. Lett.*, 2022, **33**, 4313–4316.
42 Z. Li, Q. Li, C. Li and Y. Xie, *Mater. Chem. Front.*, 2024, **8**, 652–680.
43 J. Luo, Q. Lu, Q. Li, Z. Li, Y. Wang, X. Wu, C. Li and Y. Xie, *ACS Appl. Mater. Interfaces*, 2023, **15**, 41569–41579.
44 P. Naik, K. S. Keremane, M. R. Elmorsy, R. Su and A. V. Adhikari, *Sol. Energy*, 2018, **169**, 386–391.
45 J. M. Cole, G. Pepe, O. K. Al Bahri and C. B. Cooper, *Chem. Rev.*, 2019, **119**, 7279–7327.
46 I. M. Abdellah, O. S. Zaky and M. R. Eletmany, *Opt. Mater.*, 2023, **145**, 114454.
47 C. L. Lee, W. H. Lee and C. H. Yang, *Int. J. Photoenergy*, 2013, 250397, DOI: **10.1155/2013/250397**.
48 K. S. Keremane, M. R. Eletmany, I. M. Abdellah, P. Naik and A. V. Adhikari, *J. Photochem. Photobiol., A*, 2025, **466**, 116368.
49 M. K. Nazeeruddin, A. Kay, I. Rodicio, R. Humphry-Baker, E. Mueller, P. Liska, N. Vlachopoulos and M. Graetzel, *J. Am. Chem. Soc.*, 1993, **115**, 6382–6390.
50 P. Wang, C. Klein, R. Humphry-Baker, S. M. Zakeeruddin and M. Grätzel, *J. Am. Chem. Soc.*, 2005, **127**, 808–809.
51 A. Yella, C. L. Mai, S. M. Zakeeruddin, S. N. Chang, C. H. Hsieh, C. Y. Yeh and M. Grätzel, *Angew. Chem., Int. Ed.*, 2014, **53**, 2973–2977.
52 Y. Qin and Q. Peng, *Int. J. Photoenergy*, 2012, **21**, 291579.
53 M. R. Elmorsy, R. Su, E. Abdel-Latif, S. A. Badawy, A. El-Shafei and A. A. Fadda, *J. Mater. Sci.: Mater. Electron.*, 2020, **31**, 7981–7990.
54 A. F. Buene and D. M. Almenningen, *J. Mater. Chem. C*, 2021, **9**, 11974–11994.
55 K. S. Keremane, I. M. Abdellah, P. Naik, A. El-Shafei and A. V. Adhikari, *Phys. Chem. Chem. Phys.*, 2020, **22**, 23169–23184.
56 P. Naik, N. Swain, R. Naik, N. Devarajan, D. Alagarasan and H. B. Shivaprasad, *Heliyon*, 2024, **10**(4), e25624.
57 K. A. Kumar, J. Manonmani and J. Senthilselvan, *Mater. Electron.*, 2014, **25**, 5296–5301.
58 C.-L. Lee, W.-H. Lee and C.-H. Yang, *J. Mater. Sci.*, 2013, **48**, 3448–3453.
59 K. S. Keremane and A. V. Adhikari, *J. Org. Chem. Synthesis Proc. Develop.*, 2021, **1**, 1–9.
60 P. Naik, L. Elias, K. S. Keremane, D. D. Babu and I. M. Abdellah, *Energy Technol.*, 2024, **12**, 2301666.
61 D. P. Hagberg, J. H. Yum, H. Lee, A. F. De, T. Marinado, K. M. Karlsson, R. Humphry-Baker, L. Sun, A. Hagfeldt and M. Grätzel, *J. Am. Chem. Soc.*, 2008, **130**, 6259–6266.
62 K. S. Keremane, R. Rao and A. V. Adhikari, *Photochem. Photobiol.*, 2021, **97**(2), 289–300.
63 K. S. Keremane, Y. Pellegrin, A. Planchat, D. Jacquemin, F. Odobel and A. V. Adhikari, *J. Phys. Chem. C*, 2022, **126**, 12383–12390.
64 S. Aghazada, P. Gao, A. Yella, G. Marotta, T. Moehl, J. Teuscher, J. E. Moser, A. F. De, M. Grätzel and M. K. Nazeeruddin, *Inorg. Chem.*, 2016, **55**, 6653–6659.
65 A. U. Rahman, M. B. Khan and M. Y. Rahman, *ACS Omega*, 2021, **6**(42), 27640–27653.
66 W. C. Chen, S. Nachimuthu and J. C. Jiang, *Sci. Rep.*, 2017, **7**, 4979.
67 I. M. Abdellah, A. I. Koraiem and A. El-Shafei, *Dyes Pigm.*, 2019, **164**, 244–256.
68 J. Wiberg, T. Marinado, D. P. Hagberg, L. Sun, A. Hagfeldt and B. Albinsson, *J. Phys. Chem. C*, 2009, **113**, 3881–3886.
69 B. Hosseinzadeh, A. Salimi Beni, A. Najafi Chermahini, R. Ghahary and A. Teimouri, *Synth. Met.*, 2015, **209**, 1–10.
70 N. Kaur, M. Kaur, H. S. Sohal, H. Han and P. K. Bhowmik, *Organics*, 2024, **5**, 298–345.
71 H. M. El-Shafeai, S. A. Badawy, M. A. Ismail, E. Abdel-Latif, A. A. Fadda and M. R. Elmorsy, *RSC Adv.*, 2023, **13**, 9720–9731.
72 R. Brisse, C. Praveen, V. Maffeis, T. Bourgeteau, D. Tondelier, T. Berthelot, B. Geffroy, T. Gustavsson, J. M. Raimundo and B. Jousselme, *Sustainable Energy Fuels*, 2018, **2**, 648–654.
73 P. Naik, N. Pilicode, K. S. Keremane, M. Acharya and A. V. Adhikari, *Opt. Mater.*, 2023, **142**, 114002.
74 Ji Zou, Q. Yan, C. Li, Y. Lu, Z. Tong and Y. Xie, *ACS Appl. Mater. Interfaces*, 2020, **12**(51), 57017–57024.
75 D. D. Babu, R. Su, A. El-Shafei and A. V. Adhikari, *RSC Adv.*, 2016, **6**, 30205–30216.
76 L.-Y. Lin, C.-H. Tsai, K.-T. Wong, T.-W. Huang, C.-C. Wu, S.-H. Chou, F. Lin, S.-H. Chen and A.-I. Tsai, *J. Mater. Chem.*, 2011, **21**, 5950–5958.
77 Q. Wang, J.-E. Moser and M. Grätzel, *J. Phys. Chem. B*, 2005, **109**, 14945–14953.
78 A. Sacco, *Renewable Sustainable Energy Rev.*, 2017, **79**, 814–829.
79 S. Sarker, A. J. S. Ahammad, H. W. Seo and D. M. Kim, *Int. J. Photoenergy*, 2014, 851705, DOI: **10.1155/2014/851705**.